Journal Title
XX(X):1–17

DOI: 10.1177/ToBeAssigned
www.sagepub.com/
SAGE

Adaptive Bias and Attitude Observer on the Special Orthogonal Group for True-North Gyrocompass Systems: Theory and Preliminary Results

Andrew R. Spielvogel[1] and Louis L. Whitcomb[1]

Abstract

This paper reports an adaptive sensor bias observer and attitude observer operating directly on $SO(3)$ for true-North gyrocompass systems that utilize six-degree of freedom inertial measurement units (IMUs) with three-axis accelerometers and three-axis angular rate gyroscopes (without magnetometers). Most present-day low-cost robotic vehicles employ attitude estimation systems that employ micro-electromechanical systems (MEMS) magnetometers, angular rate gyros, and accelerometers to estimate magnetic attitude (roll, pitch, and magnetic heading) with limited heading accuracy. Present day MEMS gyros are not sensitive enough to dynamically detect the Earth's rotation, and thus cannot be used to estimate true-North geodetic heading. Relying on magnetic compasses can be problematic for vehicles which operate in environments with magnetic anomalies and those requiring high accuracy navigation as the limited accuracy ($> 1^\circ$ error) of magnetic compasses is typically the largest error source in underwater vehicle navigation systems. Moreover, magnetic compasses need to undergo time-consuming recalibration for hard-iron and soft-iron errors every time a vehicle is reconfigured with a new instrument or other payload, as very frequently occurs on oceanographic marine vehicles. In contrast, the gyrocompass system reported herein utilizes fiber optic gyroscope (FOG) IMU angular rate gyro and MEMS accelerometer measurements (without magnetometers) to dynamically estimate the instrument's time-varying true-North attitude (roll, pitch, and geodetic heading) in real-time while the instrument is subject to a priori unknown rotations. This gyrocompass system is immune to magnetic anomalies and does not require recalibration every time a new payload is added to or removed from the vehicle. Stability proofs for the reported bias and attitude observers, preliminary simulations, and a full-scale vehicle trial are reported that suggest the viability of the true-North gyrocompass system to provide dynamic real-time true-North heading, pitch, and roll utilizing a comparatively low-cost FOG IMU.

Keywords

Adaptive Systems, Sensor Bias, Observer, True-north, Attitude, Gyrocompass, SO(3), Special Orthogonal Group, Lyapunov, FOG, IMU, Fiber-Optic Gyroscopes, Inertial Measurement Units, Sensor Fusion, Attitude and Heading Reference System, AHRS

1 Introduction

This paper reports a novel algorithm for estimating true-North attitude with real-time adaptive bias estimation of a *dynamic* (rotating) inertial measurement unit (IMU) *without* use of magnetometers or *a priori* knowledge of the instrument's attitude. Preliminary simulation and experimental results of the reported true-North gyrocompass system employing a low-cost fiber optic gyroscope (FOG) IMU are reported.

The current paper differs from previous work (Spielvogel and Whitcomb (2018)) by presenting a new formulation of the sensor bias estimation which relies on fewer assumptions, generalizing the attitude algorithm to be used with general field vector measurements, presenting asymptotic stability proofs for the proposed observers, and providing an approach for choosing observer gains.

1.1 *Background and Motivation*

Accurate sensing and estimation of true-North geodetic heading and local level (roll and pitch) referenced to the local gravitational field (which we will refer to as true-North attitude) are critical components of high-accuracy navigation systems for a wide variety of robotic vehicles. The need for accurate true-North attitude estimation is particularly acute in the case of vehicles operating in global positioning system (GPS)-denied environments (such as underwater) and in magnetically compromised environments (such as near ferromagnetic structures, buildings, or natural local magnetic anomalies). Smaller and lower-cost vehicles represent an additional challenge due to their limited sensor budget, small physical size, and limited energy storage capacity.

Over the past decade the development of a new generation of small low-cost underwater vehicles (UVs) has begun

[1]The Department of Mechanical Engineering, Johns Hopkins University, USA

Corresponding author:
Louis L. Whitcomb, Johns Hopkins University Dynamical Systems and Control Laboratory, Baltimore, MD, USA.
Email: llw@jhu.edu

	IMU Grade	Accel. Type	Accel. Bias	Ang. Rate Sensor	Ang. Drift	Magnetometer	Size, Weight, Power	Cost
(A)	High-End FOG/RLG	Mass	$\sim 1 - 10\mu$G	Optical	$< 1°$/h	N/A	5250 cm^3 4.5kg 14W	~$135K
(B)	Low-Cost FOG	MEMS	$\sim$ 1mG	Optical	$< 1°$/h	N/A	650 cm^3 0.7kg <5W	~$19K
(C)	MEMS	MEMS	~1 mG	MEMS	$> 10°$/h	0.01 G	12 cm^3 18g 0.4W	~$2K

Table 1. Comparison of (A) Conventional Navigation-Grade FOG/RLG IMU, (B) Low-Cost FOG IMU, and (C) MEMS IMU Specifications. (A-B) are two classes of IMUs suitable for true-North gyrocompasses, and (C) are MEMS IMUs which do not have angular rate gyros sensitive enough to be used for true-North gyrocompass systems.

to enable oceanographic, environmental assessment, and national security missions that were previously considered impractical or infeasible (e.g. Clegg and Peterson (2003); Clem et al. (2012); Packard et al. (2013); Steele et al. (2012); Zhou et al. (2014)). This new generation of UVs often employ low-cost navigation systems that presently limit them to missions requiring only low-precision navigation of $\mathcal{O}$(1-100)m accuracy when submerged. High-end navigation approaches, of $\mathcal{O}$(0.1-10)m accuracy, traditionally require a Doppler sonar, costing $20k-$50k USD, and a North-seeking gyrocompass or inertial navigation system (INS), costing $50k-$250k. These high-end navigation approaches are largely incompatible with low-cost autonomous underwater vehicles (AUVs) with target total vehicle cost of $50k-$250k. Moreover, the high cost, large size, and high power-consumption of commercially available optical true-North seeking gyrocompasses is a principal barrier to the widespread use of high accuracy navigation for smaller and lower-cost UVs.

Most small low-cost UVs typically employ micro-electro-mechanical systems (MEMS) IMUs comprised of 3-axis MEMS magnetometers, gyros, and accelerometers to estimate local magnetic heading, pitch, and roll, typically to within several degrees of accuracy, but require careful soft-iron and hard-iron calibration and compensation to achieve these accuracies. Moreover, magnetic attitude sensors must be recalibrated for soft-iron and hard-iron errors whenever the vehicle's physical configuration changes significantly (i.e. sensors or other payloads added or removed, etc.), as very frequently occurs on oceanographic marine vehicles. Studies have shown that the accuracy of these magnetic heading sensors can be a principal error source in overall navigation solutions (Kinsey and Whitcomb (2004)).

Recently, a new class of lower-cost (~$20k), compact, and lower power FOG IMUs have become available — for example the commercial-off-the-shelf (COTS) KVH 1775 FOG IMU (KVH Industries, Inc., Middletown, RI, USA) — that provide sensor accuracies sufficient for estimation of true-North heading, pitch, and roll. This is in contrast to MEMS IMUs, which employ MEMS gyros that lack the sensitivity necessary to detect Earth-rate, and hence true-North heading, and thus rely on MEMS magnetometers to sense magnetic heading.

1.2 True-North Versus Magnetic Heading

True-North heading estimation differs from that of magnetic heading in that true-North is the direction towards the Earth's axis of rotation at the North Pole, while magnetic heading measures the direction of the horizontal component of the Earth's local magnetic field, which differs dramatically from true-North, often by many 10's of degrees — a difference termed *local magnetic variation*. The gyroscope sensors (includes all MEMS IMUs) used in magnetic-North attitude sensors typically lack the sensitivity (the magnitude of Earth rate is orders of magnitude smaller than the magnitude of MEMS angular rate gyro sensor noise) to detect the angular rate of Earth (15°/hr) and are commonly modeled as

$$w_m(t) = \cancelto{0}{w_E(t)} + w_v(t) + w_b + \eta(t) \tag{1}$$

where $w_m(t) \in \mathbb{R}^3$ is the measured angular rate vector in instrument coordinates, $w_E(t) \in \mathbb{R}^3$ is the angular rate of the Earth (15°/hr), $w_v(t) \in \mathbb{R}^3$ is the angular rate of the instrument with respect to the local North, East, Down frame, $w_b \in \mathbb{R}^3$ is a constant measurement bias, and $\eta(t) \in \mathbb{R}^3$ is zero-mean Gaussian measurement noise. In contrast, true-North gyrocompass systems use high-end gyroscopes, such as three-axes FOGs or ring laser gyros (RLGs), which are sensitive enough ($\|w_E(t)\| \gtrsim \|\eta(t)\|$) to measure Earth's angular rate and are typically modeled as

$$w_m(t) = w_E(t) + w_v(t) + w_b + \eta(t) \tag{2}$$

where the terms are the same as in (1). Table 1 compares these different classes of IMUs.

By fusing gyroscope and accelerometer measurements, true-North gyrocompass systems generate an estimate for the $w_E(t)$ component of the measured angular rate $w_m(t)$. Since the Earth's angular rate, $w_E(t)$, lies in the local North-down plane, the estimated angular-rate of Earth ($w_E(t)$) and the estimated gravity vector can be fused to estimate the true-North direction, roll, and pitch. We define the local North-down plane to be the plane that intersects the origin of the NED frame (defined in Section 3.1) and spans the North and down directions.

1.3 Paper Organization

This paper is organized as follows: Section 2 provides a literature review of attitude and sensor bias estimation. Section 3 gives an overview of preliminaries. Section 4 reports the sensor bias and East vector observer and stability proof. Section 5 presents the attitude observer and stability proof. Section 6 introduces the Gyrocompass system. Section 7 presents preliminary numerical simulations and experimental results. Section 8 summarizes and concludes.

2 Literature Review

Because field sensors, such as angular rate gyros and accelerometers, have significant sensor bias terms that typically vary strongly with instrument temperature and otherwise drift very slowly over time, it is necessary to simultaneously estimate field sensor bias terms AND estimate attitude. Section 2.1 reviews relevant literature on attitude estimation, and Section 2.2 reviews relevant literature on IMU sensor bias estimation.

2.1 Attitude Estimation

The majority of the attitude estimation literature addresses the case of magnetic heading attitude estimation using MEMS IMUs (Crassidis et al. (2007); Guo et al. (2008); Hamel and Mahony (2006); Metni et al. (2005, 2006); Wu et al. (2015)). Mahony et al. (2008) report an attitude nonlinear complementary filter on $SO(3)$. A recent study by Costanzi et al. (2016) explores utilizing a FOG for attitude estimation under unknown magnetic disturbances. These studies however, differ from the current paper as they estimate magnetic-North heading, while the present paper presents an estimator for true-North heading.

Martinelli (2012) reports a method for estimating roll and pitch using a three-axis accelerometer and three-axis gyroscope IMU and a monocular camera. This approach however is impractical for many UV applications (e.g. when there is poor visibility due to water turbidity, operating in the mid-water, operating in a region with a featureless bottom) and impossible for the many unmanned underwater vehicles (UUVs) that are not equipped with cameras and lights/strobes.

Previous studies by Spielvogel and Whitcomb (2015, 2017a) suggest the practical utility of a low-cost FOG IMU as the primary sensor in a North-seeking gyrocompass system. These studies assume that sensor biases have been calculated and compensated for *a priori* and rely on the differentiation of accelerometer measurements for estimating true-North. Numerical simulation and experimental evaluations are reported.

Batista et al. (2019) report a nonlinear attitude observer based upon angular rate gyros and single body-fixed vector measurements of a constant "inertial vector" (e.g. 3-axis magnetometer) where the gyros and fixed-vector sensor are all assumed to be bias-free. A numerical simulation evaluation is reported.

Spielvogel and Whitcomb (2018) present a true-North gyrocompass system which estimates true-North attitude without the need to differentiate accelerometer measurements and also addresses the problem of real time bias estimation for both gyros and accelerometers. The current paper differs from the previous attitude observer by generalizing the algorithm to be used with general field vector measurements and provides a local asymptotic stability proof and observability analysis. Numerical simulation and experimental evaluations are reported.

2.2 IMU Sensor Bias Estimation

Several methods for IMU measurement bias estimation have been reported in recent years. Much of this literature, though, focuses on magnetometer bias estimation (Alonso and Shuster (2002b,a); Crassidis et al. (2005); Gambhir (1975); Guo et al. (2008); Kok et al. (2012); Li and Li (2012); Troni and Whitcomb (2013); Troni and Whitcomb (2019); Spielvogel and Whitcomb (2018)).

Many papers report results for gyro sensor bias estimation. However, most address MEMS gyro sensor bias estimation

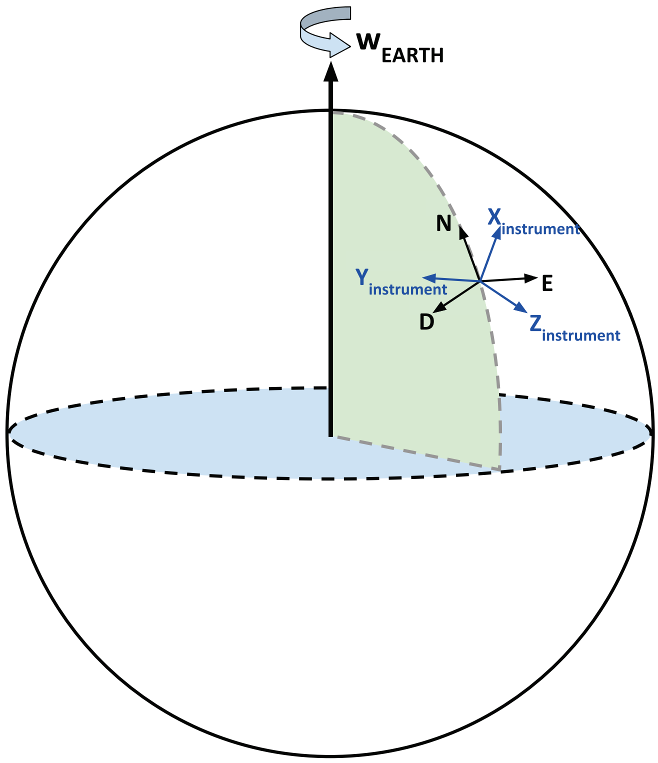

Figure 1. The North-East-Down (NED) and instrument coordinate frames are co-located.

in which the angular rate due to Earth's rotation is ignored in the gyro measurement model. They use a measurement model similar to that of (1) and neglect the Earth rate term because Earth rate is dynamically undetectable with MEMS gyros.

George and Sukkarieh (2005) report an identifier for accelerometer and gyroscope sensor bias. However, they utilize GPS which is unavailable to submerged vehicles.

Scandaroli and Morin (2011) and Scandaroli et al. (2011) also report a sensor bias estimator for 6-degrees of freedom (DOF) IMUs utilizing computer vision. This method though is dependent on the presence of a vision system, which requires identification markers in the environment and a camera system which is unavailable for many robotic vehicles (e.g. many underwater vehicles).

Metni et al. (2005, 2006) and Pflimlin et al. (2007) report nonlinear complementary filters for estimating attitude and gyroscope sensor bias. While these estimators identify angular-rate sensor bias, they do not address linear acceleration sensor bias and do not distinguish the gyroscope sensor bias from Earth's angular velocity.

Spielvogel and Whitcomb (2017b) addresses the problem of identifying and distinguishing the gyro bias from the Earth-rate signal. However, this reported approach requires knowledge of the instrument's real-time attitude.

Spielvogel and Whitcomb (2018) reports an adaptive sensor bias and north observer to be used in a true-North gyrocompass system *without a priori* knowledge of the instrument's attitude. The present paper differs from this previous work by presenting a new formulation of the sensor bias estimation which relies on fewer assumptions, a proof of asymptotic stability (instead of only stability), and an approach for choosing observer gains.

3 Preliminaries

3.1 Coordinate Frames

We define the following coordinate frames:

- **Instrument Frame:** A frame, denoted (i), fixed in the IMU instrument.
- **North-East-Down (NED) Frame:** The North-East-Down (NED) frame, denoted (N), has its x-axis pointing True-North, its y-axis pointing East, its z-axis pointing down, and its origin co-located with that of the instrument frame.

Figure 1 illustrates these two coordinate frames.

3.2 Notation and Definitions

For each vector, a leading superscript indicates the frame of reference and a following subscript indicates the signal source, thus ${}^{N}w_m$ is the measured instrument angular velocity in the NED frame and ${}^{i}a_m$ is the measured instrument linear acceleration in the instrument sensor frame.

For each rotation matrix a leading superscript and subscript indicates the frames of reference. For example, ${}^{N}_{i}R$ is the rotation from the instrument frame to the NED frame.

Definition: $\mathcal{J}$ is defined as a function that maps a 3×1 vector to the corresponding 3×3 skew-symmetric matrix, $\mathcal{J} : \mathbb{R}^3 \rightarrow so(3)$. For $k \in \mathbb{R}^3$,

$$\mathcal{J}(k) = \begin{bmatrix} 0 & -k_3 & k_2 \\ k_3 & 0 & -k_1 \\ -k_2 & k_1 & 0 \end{bmatrix}. \tag{3}$$

We define its inverse $\mathcal{J}^{-1} : so(3) \rightarrow \mathbb{R}^3$, such that $\forall x \in \mathbb{R}^3$, $\mathcal{J}^{-1}(\mathcal{J}(x)) = x$.

3.3 Mathematical Background

We will make use of the following mathematical facts:

Proposition: For $Q(t) \in so(3)$, the rotation matrix $R(t)$ can be computed by Rodrigues Equation (Murray et al. (1994))

$$R(t) = I_{3\times3} + \gamma(t)Q(t) + \kappa(t)Q(t)^2 \tag{4}$$

where

$$\gamma(t) = \frac{\sin(\|q(t)\|)}{\|q(t)\|} \tag{5}$$

$$\kappa(t) = \frac{1 - \cos(\|q(t)\|)}{\|q(t)\|^2} \tag{6}$$

$$q(t) = \mathcal{J}^{-1}(Q(t)). \tag{7}$$

Proposition: $\dot{q}(t)$ is related to $\dot{R}(t)$ by the mapping

$$R^T(t)\dot{R}(t) = \mathcal{J}(A(q(t))\dot{q}(t)) \tag{8}$$

where $A(q(t))$ is the right Jacobian of $R(t) = e^{\mathcal{J}(q(t))}$ with respect to the angular position vector $q(t) \in \mathbb{R}^3$. $A(q(t))$:

$$A\left(q(t)\right) = I_{3\times3} - \phi(t)\mathcal{J}\left(q(t)\right) + \psi(t)\mathcal{J}^2\left(q(t)\right) \tag{9}$$

$$\phi(t) = \frac{1 - \cos\left(\|q(t)\|\right)}{\|q(t)\|^2} \tag{10}$$

$$\psi(t) = \frac{\|q(t)\| - \sin\left(\|q(t)\|\right)}{\|q(t)\|^3} \tag{11}$$

and its inverse,

$$A^{-1}(q(t)) = I_{3\times3} + \alpha\mathcal{J}(q(t)) + \beta(t)\mathcal{J}^2(q(t)) \tag{12}$$

where

$$\alpha = \frac{1}{2}, \tag{13}$$

$$\beta(t) = \frac{1}{\|q(t)\|^2} - \frac{1 + \cos(\|q(t)\|)}{2\|q(t)\|\sin(\|q(t)\|)}, \tag{14}$$

are reported in Chirikjian (2011).

If $A(q(t))$ is invertible, (8) can be rearranged as

$$\dot{q}(t) = A^{-1}\left(q(t)\right)\mathcal{J}^{-1}\left(R^T(t)\dot{R}(t)\right). \tag{15}$$

Definition: Persistent Excitation (PE)) (Sastry and Bodson (1989)) A matrix function $\mathcal{W} : \mathbb{R}^+ \rightarrow \mathbb{R}^{m\times n}$ is persistently exciting (PE) if there exist $T, \alpha_1, \alpha_2 > 0$ such that $\forall t \geq 0$:

$$\alpha_1 I_m \geq \int_t^{t+T} \mathcal{W}(\tau)\mathcal{W}^T(\tau)\, d\tau \geq \alpha_2 I_m \tag{16}$$

where $I_m \in \mathbb{R}^{m\times m}$ is the identity matrix.

Definition: Uniform Complete Observability (UCO) (Sastry and Bodson (1989)) The system $[A(t), C(t)]$ is called uniformly completely observable (UCO) if there exist strictly positive constants β_1, β_2, δ, such that, $\forall t_0 \geq 0$

$$\beta_2 I \geq N(t_0, \delta) \geq \beta_1 I \tag{17}$$

where $N(t_0, \delta) \in \mathbb{R}^{n\times n}$ is the observability grammian

$$N(t_0, \delta) = \int_{t_0}^{t_0+\delta} \Phi^T(\tau, t_0)C^T(\tau)C(\tau)\Phi(\tau, t_0)\, d\tau \tag{18}$$

and $\Phi(t, t_0)$ is the transition matrix for $A(t)$ (Rugh (1996)).

Lemma 1 : The following lemma is a variation of Lemma A.1 in (Besançon (2000)). Given a system of the following form:

$$\dot{x}(t) = A(t)x(t) + f(t) \tag{19}$$

$$y(t) = Cx(t) \tag{20}$$

where $x(t) \in \mathbb{R}^n$, and $y(t) \in \mathbb{R}^p$ such that

(i) $\lim_{t\to\infty} \|y(t)\| = 0$

(ii) $\lim_{t\to\infty} \|f(t)\| = 0$

(iii) $[A(t), C]$ is UCO;

then $\lim_{t\to\infty} \|x(t)\| = 0$. Proof provided in Appendix 1.

3.4 Sensor Model

The sensor measurement models for angular rate and linear acceleration are

$${}^{i}w_e(t) = {}^{i}w_E(t) + {}^{i}w_v(t) + {}^{i}w_b \tag{21}$$

$${}^{i}w_m(t) = {}^{i}w_e(t) + {}^{i}\eta_w(t) \tag{22}$$

$${}^{i}a_e(t) = {}^{i}a_g(t) + {}^{i}a_v(t) + {}^{i}a_b \tag{23}$$

$${}^{i}a_m(t) = {}^{i}a_e(t) + {}^{i}\eta_a(t) \tag{24}$$

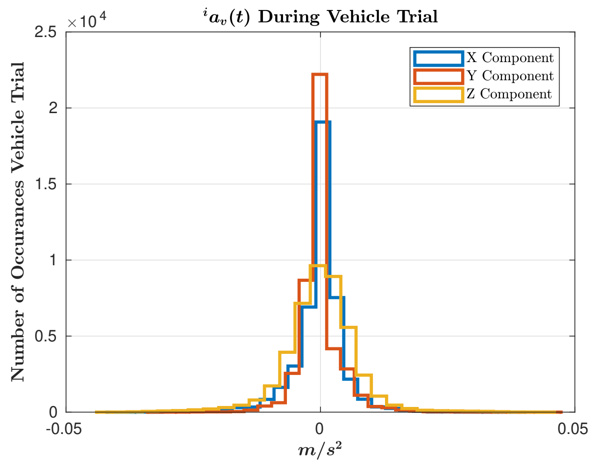

Figure 2. Histogram of the components of the vehicle acceleration experience by the Johns Hopkins University (JHU) remotely operated vehicle (ROV) during the vehicle trial. The vehicle acceleration data is from the high-end PHINS INS on the JHU ROV. As shown above, the vehicle experiences vehicle accelerations which are orders of magnitude smaller than gravity ($<< 9.81 \ m/s^2$).

where ${}^{i}w_m(t) \in \mathbb{R}^3$ is the IMU measured angular-rate, ${}^{i}w_e(t) \in \mathbb{R}^3$ is the biased noise-free angular-rate, ${}^{i}w_E(t) \in \mathbb{R}^3$ is the true angular velocity due to the rotation of the Earth, ${}^{i}w_v(t) \in \mathbb{R}^3$ is the true angular velocity due to the rotation of the instrument with respect to the NED frame, ${}^{i}w_b \in \mathbb{R}^3$ is the angular velocity sensor bias offset, ${}^{i}\eta_w(t) \in \mathbb{R}^3$ is the zero-mean Gaussian angular velocity sensor noise, ${}^{i}a_m(t) \in \mathbb{R}^3$ is the IMU measured linear acceleration, ${}^{i}a_e(t) \in \mathbb{R}^3$ is the biased noise-free linear acceleration, ${}^{i}a_g(t) \in \mathbb{R}^3$ is the true linear acceleration due to gravity and the Earth's rotation, ${}^{i}a_v(t)$ is the instrument's true linear acceleration with respect to Earth, ${}^{i}a_b \in \mathbb{R}^3$ is the linear accelerometer sensor bias, and ${}^{i}\eta_a(t) \in \mathbb{R}^3$ is the zero-mean Gaussian linear accelerometer sensor noise.

For many robotic vehicles, the gravitational field ${}^{i}a_g(t)$ dominates the vehicle linear acceleration (${}^{i}a_v(t)$). Thus, it is common to use the approximation

$$ {}^{i}a_e(t) \approx {}^{i}a_g(t) + {}^{i}a_b \tag{25} $$

as a low-frequency estimate of (23). This approximation, (25), is used in (Costanzi et al. (2016); Mahony et al. (2008); Pflimlin et al. (2007); Wu et al. (2015)). Figure 2 presents the vehicle acceleration experienced by the JHU ROV in the vehicle trial. From Figure 2, it is evident that the magnitude of the vehicle accelerations experienced in the vehicle trial are orders of magnitude smaller than the gravity vector.

Given (25), the sensor measurement model becomes

$$ {}^{i}w_e(t) = {}^{i}w_E(t) + {}^{i}w_v(t) + {}^{i}w_b \tag{26} $$
$$ {}^{i}w_m(t) = {}^{i}w_e(t) + {}^{i}\eta_w(t) \tag{27} $$
$$ {}^{i}a_e(t) = {}^{i}a_g(t) + {}^{i}a_b \tag{28} $$
$$ {}^{i}a_m(t) = {}^{i}a_e(t) + {}^{i}\eta_a(t). \tag{29} $$

Section 7.6 shows the proposed algorithms perform well in the experimental trial where the vehicle experienced small vehicle accelerations ($\|{}^{i}a_v(t)\| \approx 0$), thus empirically justifying the neglection of the vehicle acceleration term ${}^{i}a_v(t)$ in (25) for a slowly accelerating vehicle.

4 Sensor Bias and East Observer

This section reports the derivation and stability analysis of an adaptive sensor bias and East vector observer for six-DOF IMUs equipped with a three-axis accelerometer and three-axis angular rate gyroscope. The field sensor biases are assumed to be very slowly time varying, and hence we model them as constant terms and update their estimates continuously.

Note that to estimate true-North heading, the angular rate gyroscope must be sensitive enough to detect Earth-rate. The measurement noise of present-day angular rate gyros in MEMS IMUs is orders of magnitude larger than what is needed to detect the extremely minute signal of the Earth's rotation rate (15°/hr), thus, MEMS IMUs cannot be utilized to dynamically estimate directly true-North heading. At present, true-North attitude can only be successfully instrumented with high-end, angular-rate gyros that employ RLG or FOG angular rate sensors, or that employ large inertial-grade mechanical gyrocompasses. Although high-end angular-rate gyros are necessary for true-North gyrocompasses, the systems do not simply employ a better IMU (more precise, without ferromagnetic disturbances) to obtain more precise results using common algorithms utilizing magnetic heading sensors, but rather use the local gravity vector and Earth's rotation axis for estimating true-North attitude. This is impossible with an IMU that is not sensitive enough to detect Earth's rotation.

The present paper reports a system that successfully estimates true-North attitude utilizing a new class of compact, low-power, and lower cost FOG IMUs.

4.1 System Model

We consider the system model

$$ {}^{N}a_g = {}^{N}_{i}R(t)\,{}^{i}a_g(t) \tag{30} $$
$$ {}^{N}e = {}^{N}_{i}R(t)\,{}^{i}e(t) \tag{31} $$

where the "East" vector,

$$ {}^{i}e(t) = \mathcal{J}\left({}^{i}w_E(t)\right){}^{i}a_g(t), \tag{32} $$

is defined as the cross product of the Earth's rotation axis with the local gravity vector. Note that the proposed observer will not work well near polar regions where the local gravity vector is close to collinear with the Earth's rotation axis.

Since ${}^{N}a_g$ and ${}^{N}e$ are constant in the NED frame, differentiating (30) and (31), rearranging terms, and substituting (26) yields

$$ {}^{i}\dot{a}_g(t) = -\mathcal{J}\left({}^{i}w_e(t) - {}^{i}w_b - {}^{i}w_E(t)\right){}^{i}a_g(t) \tag{33} $$
$$ {}^{i}\dot{e}(t) = -\mathcal{J}\left({}^{i}w_e(t) - {}^{i}w_b - {}^{i}w_E(t)\right){}^{i}e(t). \tag{34} $$

From (28), we know that

$$ {}^{i}a_g(t) = {}^{i}a_e(t) - {}^{i}a_b \tag{35} $$
$$ {}^{i}\dot{a}_g(t) = {}^{i}\dot{a}_e(t) - {}^{i}\dot{a}_b = {}^{i}\dot{a}_e(t). \tag{36} $$

Substituting (28), (32), and (36) into (33) and (34) results in

$$\begin{aligned} {}^i\dot{a}_e(t) &= -\mathcal{J}\left({}^iw_e(t) - {}^iw_b\right){}^ia_g(t) + {}^ie(t) \\ &= -\mathcal{J}\left({}^iw_e(t) - {}^iw_b\right)\left({}^ia_e(t) - {}^ia_b\right) + {}^ie(t). \end{aligned} \quad (37)$$

Since the cross products between sensor biases and Earth-rate are orders of magnitude smaller than the other signals, we make the approximations that $\mathcal{J}\left({}^iw_b\right){}^ia_b \approx 0$ and $\mathcal{J}\left({}^iw_b + {}^iw_E(t)\right){}^ie(t) \approx 0$. Note that for the KVH FOG IMU used in the present paper, $\|\mathcal{J}\left({}^iw_b\right){}^ia_b\|$ is order 10^{-7} and $\|\mathcal{J}\left({}^iw_b + {}^iw_E(t)\right){}^ie(t)\|$ is order 10^{-7}, while $\|\mathcal{J}\left({}^iw_e(t)\right)\left({}^ia_e(t) - {}^ia_b\right)\|$ is order $\geq 10^{-4}$, $\|\mathcal{J}\left({}^iw_b\right){}^ia_e(t)\|$ is order 10^{-1}, $\|{}^ie(t)\|$ is order 10^{-4}, and $\|\mathcal{J}\left({}^iw_e(t)\right){}^ie(t)\|$ is order $\|{}^iw_v(t)\| * 10^{-4}$.

The resulting plant is

$$\begin{aligned} {}^i\dot{a}_e(t) &= -\mathcal{J}\left({}^iw_e(t)\right)\left({}^ia_e(t) - {}^ia_b\right) \\ &\quad + \mathcal{J}\left({}^iw_b\right){}^ia_e(t) + {}^ie(t) && (38) \\ {}^i\dot{e}(t) &= -\mathcal{J}\left({}^iw_e(t)\right){}^ie(t) && (39) \\ {}^i\dot{w}_b &= 0 && (40) \\ {}^i\dot{a}_b &= 0 && (41) \\ y(t) &= {}^ia_e(t). && (42) \end{aligned}$$

4.2 Sensor Bias and East Observer

We propose the observer

$$\begin{aligned} {}^i\dot{\hat{a}}_e(t) &= -\mathcal{J}\left({}^iw_e(t)\right)\left({}^i\hat{a}_e(t) - {}^i\hat{a}_b\right) \\ &\quad + \mathcal{J}\left({}^i\hat{w}_b\right){}^i\hat{a}_e(t) + {}^i\hat{e}(t) - k_a\Delta a(t) && (43) \\ {}^i\dot{\hat{e}}(t) &= -\mathcal{J}\left({}^iw_e(t)\right){}^i\hat{e}(t) - k_e\Delta a(t) && (44) \\ {}^i\dot{\hat{w}}_b(t) &= -k_{b_w}\mathcal{J}\left({}^ia_e(t)\right)\Delta a(t) && (45) \\ {}^i\dot{\hat{a}}_b(t) &= k_{b_a}\mathcal{J}\left({}^iw_e(t)\right)\Delta a(t) && (46) \\ \hat{y}(t) &= {}^i\hat{a}_e(t) && (47) \end{aligned}$$

where k_a, k_e, k_{b_w}, and k_{b_a} are constant positive scalar gains, ${}^i\hat{a}_e(t)$, ${}^i\hat{e}(t)$, ${}^i\hat{w}_b(t)$, and ${}^i\hat{a}_b(t)$ are the estimates of ${}^ia_e(t)$, ${}^ie(t)$, ${}^iw_b$, and ${}^ia_b$ respectively, and

$$\begin{aligned} \Delta a(t) &= {}^i\hat{a}_e(t) - {}^ia_e(t) && (48) \\ \Delta e(t) &= {}^i\hat{e}(t) - {}^ie(t) && (49) \\ \Delta w_b(t) &= {}^i\hat{w}_b(t) - {}^iw_b && (50) \\ \Delta a_b(t) &= {}^i\hat{a}_b(t) - {}^ia_b && (51) \\ \Delta y(t) &= \hat{y}(t) - y(t) && (52) \end{aligned}$$

are the corresponding error terms.

Note that in the proposed algorithm, the signals ${}^iw_e(t)$ and ${}^ia_e(t)$ are the only signals in the instrument frame needed for the algorithm to work. Knowledge of ${}^Na_g$ and ${}^Nw_E$ is not needed.

4.3 Error System

The resulting error system is

$$\begin{aligned} \Delta\dot{a}(t) &= -\mathcal{J}\left({}^iw_e(t)\right)\Delta a(t) + \mathcal{J}\left({}^iw_e(t)\right)\Delta a_b(t) \\ &\quad + \mathcal{J}\left({}^i\hat{w}_b(t)\right)\Delta a(t) - \mathcal{J}\left({}^ia_e(t)\right)\Delta w_b(t) \\ &\quad + \Delta e(t) - k_a\Delta a(t) && (53) \\ \Delta\dot{e}(t) &= -\mathcal{J}\left({}^iw_e(t)\right)\Delta e(t) - k_e\Delta a(t) && (54) \\ \Delta\dot{w}_b(t) &= -k_{b_w}\mathcal{J}\left({}^ia_e(t)\right)\Delta a(t) && (55) \\ \Delta\dot{a}_b(t) &= k_{b_a}\mathcal{J}\left({}^iw_e(t)\right)\Delta a(t) && (56) \\ \Delta y(t) &= \Delta a(t). && (57) \end{aligned}$$

4.4 Stability

Consider the Lyapunov function candidate

$$\begin{aligned} V &= \frac{1}{2}\Delta a^T(t)\Delta a(t) + \frac{1}{2k_e}\Delta e^T(t)\Delta e(t) \\ &\quad + \frac{1}{2k_{b_w}}\Delta w_b^T(t)\Delta w_b(t) + \frac{1}{2k_{b_a}}\Delta a_b^T(t)\Delta a_b(t) \end{aligned} \quad (58)$$

where V is a smooth, positive definite, and radially unbounded function by construction. Differentiating (58) results in

$$\begin{aligned} \dot{V} &= \Delta a^T(t)\Delta\dot{a}(t) + \frac{1}{k_e}\Delta\dot{e}^T(t)\Delta e(t) \\ &\quad + \frac{1}{k_{b_w}}\Delta\dot{w}_b^T(t)\Delta w_b(t) + \frac{1}{k_{b_a}}\Delta\dot{a}_b^T(t)\Delta a_b(t) \\ &= \left(-\Delta a^T(t)\mathcal{J}\left({}^ia_e(t)\right) + \Delta a^T(t)\mathcal{J}\left({}^ia_e(t)\right)\right)\Delta w_b(t) \\ &\quad + \left(\Delta a^T(t)\mathcal{J}\left({}^iw_e(t)\right) - \Delta a^T(t)\mathcal{J}\left({}^iw_e(t)\right)\right)\Delta a_b(t) \\ &\quad + \left(\Delta a^T(t) - \Delta a^T(t)\right)\Delta e(t) \\ &\quad + \frac{1}{k_e}\Delta e^T(t)\mathcal{J}\left({}^iw_e(t)\right)\Delta e(t) \\ &\quad + \Delta a^T(t)\mathcal{J}\left({}^i\hat{w}_b(t) - {}^iw_e(t)\right)\Delta a(t) \\ &\quad - k_a\Delta a^T(t)\Delta a(t) \\ &= -k_a\|\Delta a(t)\|^2 \\ &\leq 0. \end{aligned} \quad (59)$$

Since k_a is a positive scalar, the time derivative of the Lyapunov function is negative semidefinite and the observer is globally stable.

Since (58) is radially unbounded, bounded below by 0, and bounded above by its initial value, $V(t_0)$, due to (59), we can conclude that $\Delta a(t)$, $\Delta e(t)$, $\Delta w_b(t)$, and $\Delta a_b(t)$ are bounded. If we make the assumption that the signals ${}^ia_e(t)$, ${}^iw_e(t)$, ${}^iw_b$, and ${}^ia_b$ are bounded, then (53)-(57) are bounded, and hence (48)-(51) are uniformly continuous.

For all $t \geq 0$,

$$\begin{aligned} -\int_{t_0}^{t}\dot{V}(\tau)\,d\tau &= \int_{t_0}^{t}k_a\|\Delta a(\tau)\|^2\,d\tau \\ V(t_0) - V(t) &= k_a\int_{t_0}^{t}\|\Delta a(\tau)\|^2\,d\tau \\ V(t_0) &= k_a\int_{t_0}^{t}\|\Delta a(\tau)\|^2\,d\tau + V(t). \end{aligned} \quad (60)$$

Since $V(t) \geq 0 \; \forall t > t_0$, (60) can be written as

$$k_a \int_{t_0}^{t} \|\Delta a(\tau)\|^2 \, d\tau \leq V(t_0)$$
$$\left(\int_{t_0}^{t} \|\Delta a(\tau)\|^2 \, d\tau \right)^{1/2} \leq \left(\frac{V(t_0)}{k_a} \right)^{1/2}. \quad (61)$$

Hence, $\Delta a(t) \in L^2$ (Khalil (1996)).

Since $\Delta a(t) \in L^2 \cap L^\infty$ and $\Delta \dot{a}(t)$ is bounded, from Corollary 2.9 in (Narendra and Annaswamy (1989)), we conclude that $\Delta a(t)$ is globally asymptotically stable at the origin,

$$\lim_{t \to \infty} \Delta a(t) = 0. \quad (62)$$

Note that we can rewrite the error system into the form

$$\dot{\theta}(t) = A(t)\theta(t) + f(t) \quad (63)$$
$$y(t) = C\theta(t) \quad (64)$$

where

$$\theta(t) = \begin{bmatrix} \Delta a(t) \\ \Delta e(t) \\ \Delta w_b(t) \\ \Delta a_b(t) \end{bmatrix}, \quad (65)$$
$$A(t) = \begin{bmatrix} 0 & g(t) \\ 0 & 0 \end{bmatrix}, \quad (66)$$
$$g(t) = \begin{bmatrix} I & -\mathcal{J}\left({}^i a_e(t)\right) & \mathcal{J}\left({}^i w_e(t)\right) \\ -\mathcal{J}\left({}^i w_e(t)\right) & 0 & 0 \end{bmatrix}, \quad (67)$$
$$f(t) = \begin{bmatrix} -\mathcal{J}\left({}^i w_e(t) - \hat{w}_b(t)\right) - k_a I \\ -k_e I \\ -k_{b_w} \mathcal{J}\left({}^i a_e(t)\right) \\ k_{b_a} \mathcal{J}\left({}^i w_e(t)\right) \end{bmatrix} \Delta a(t), \quad (68)$$
$$C = \begin{bmatrix} I & 0 & 0 & 0 \end{bmatrix}, \quad (69)$$

and $I \in \mathbb{R}^{3\times 3}$ is the identity matrix. Since $\lim_{t\to\infty} \Delta a(t) = 0$, we conclude that

(i) $\lim_{t\to\infty} \|y(t)\| = 0$

(ii) $\lim_{t\to\infty} \|f(t)\| = 0$

Thus, if $[A(t), C]$ is UCO, from Lemma 1, we conclude the error system is asymptotically stable and hence

$$\lim_{t \to \infty} \|\theta(t)\| = 0. \quad (70)$$

We conclude that, if ${}^i a_e(t), {}^i w_e(t), {}^i w_b$, and ${}^i a_b$ are bounded and $[A(t), C]$ is UCO, then the system is asymptotically stable. Note that for underwater vehicles, the signals ${}^i a_e(t), {}^i w_e(t), {}^i w_b$, and ${}^i a_b$ are all bounded (see Figure 9 for the sensor measurements from the numerical simulations and vehicle trial), so convergence of the observer is dependent on $[A(t), C]$ being UCO. In our case, where $A(t)$ depends on the coupled exogenous signals ${}^i w_e(t)$ and ${}^i a_e(t)$, it is not obvious that $\Phi(t, t_0)$ (the transition matrix for $A(t)$) has a closed-form solution for non-trivial ${}^i w_e(t)$ and ${}^i a_e(t)$, and, in consequence, it is not clear how to prove analytically that the observability grammian $N(t_0, \delta)$, defined in (18), satisfies (17). It is easy to verify numerically that when ${}^i w_e(t)$ and ${}^i a_e(t)$ are PE, $[A(t), C]$ is UCO. Conversely, it is also easy to verify numerically that when ${}^i w_e(t)$ and ${}^i a_e(t)$ are not PE, $[A(t), C]$ is not UCO. Appendix 2 reports numerical evaluations of the observability grammian for the simulation data presented in Section 7.

5 Attitude Observer

This section reports the derivation and stability analysis of an attitude observer that estimates directly on $SO(3)$. The observer is inspired in part by the research of Mahony et al. (2008) on nonlinear complementary filters on $SO(3)$ and research by Kinsey and Whitcomb (2007) on adaptive identification on $SO(3)$. The general terms x and z are used because the observer is not limited to the problem of true-North attitude estimation — it can also be applied (for example) to magnetometer-IMU systems for attitude estimation with respect to local magnetic-North.

5.1 Plant

Consider the plant

$${}^N x = {}^N_i R(t) {}^i x(t) \quad (71)$$
$${}^N z = {}^N_i R(t) {}^i z(t) \quad (72)$$

where ${}^i x(t)$ and ${}^i z(t)$ are orthogonal such that ${}^i x^T(t) {}^i z(t) = 0$. The signals ${}^N x \in \mathbb{R}^3$, ${}^i x(t) \in \mathbb{R}^3$, ${}^N z \in \mathbb{R}^3$, and ${}^i z(t) \in \mathbb{R}^3$ are known and non-zero. The rotation matrix ${}^N_i R(t) \in SO(3)$ is unknown.

5.2 Identification Plant

Define ${}^N_i \hat{R}(t) \in SO(3)$ to be the estimate of ${}^N_i R(t)$, and ${}^N \hat{x}, {}^N \hat{z} \in \mathbb{R}^3$ to be the estimated plant output

$${}^N \hat{x} = {}^N_i \hat{R}(t) {}^i x(t) \quad (73)$$
$${}^N \hat{z} = {}^N_i \hat{R}(t) {}^i z(t), \quad (74)$$

where ${}^i x(t), {}^i z(t)$ are "field vectors". In out particular instance, the field vectors are ${}^i a_g(t), {}^i e(t)$ respectively.

5.3 Parameter Error

The parameter error is defined as

$$\tilde{R}(t) = {}^N_i R^T(t) {}^N_i \hat{R}(t). \quad (75)$$

When ${}^N_i \hat{R}(t) = {}^N_i R(t)$, ${}^N_i R^T(t) {}^N_i \hat{R}(t) = I$ where I is the 3×3 identity matrix.

5.4 Attitude Observer Update Law

We choose the update law

$${}^N_i \dot{\hat{R}}(t) = {}^N_i \hat{R}(t) \mathcal{J}\left(\tilde{x}(t) + \tilde{z}(t) + {}^i w_e(t) - {}^i w_b - {}^N_i \hat{R}^T(t) {}^N w_E\right). \quad (76)$$

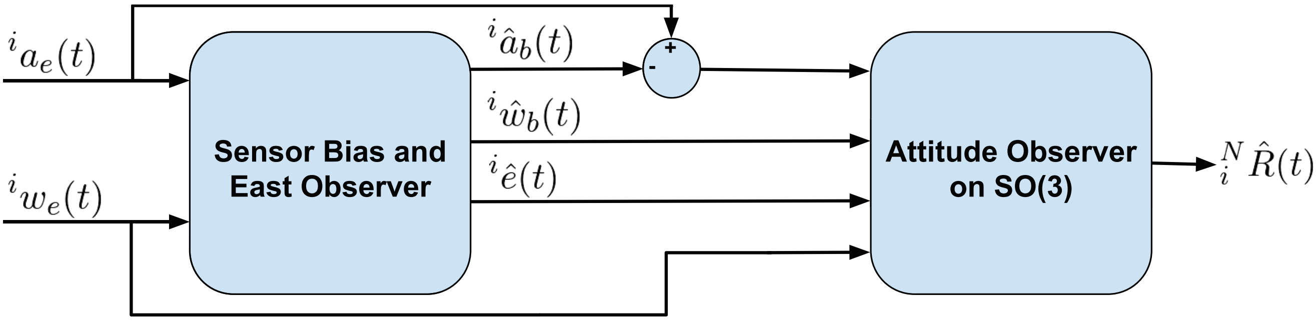

Figure 3. Block diagram of the gyrocompass system.

where the $\tilde{x}(t) \in \mathbb{R}^3$ and $\tilde{z}(t) \in \mathbb{R}^3$ are local field vector error terms defined, respectively, as

$$\tilde{x}(t) = k_x(t)\mathcal{J}\left({}^i x(t)\right){}^N_i\hat{R}^T(t)^N x \tag{77}$$

$$\tilde{z}(t) = k_z(t)\mathcal{J}\left((I - P(t))\,{}^i z(t)\right){}^N_i\hat{R}^T(t)^N z \tag{78}$$

where the projection matrix, $P(t)$, and normalized vector ${}^i\bar{x}(t)$ are defined as

$$P(t) = {}^i\bar{x}(t)^i\bar{x}^T(t), \tag{79}$$

$${}^i\bar{x}(t) = {}^i x(t)\frac{1}{\|{}^i x(t)\|}, \tag{80}$$

and $k_x(t)$ and $k_z(t)$ are positive scalar gains.

5.5 Error System

The corresponding error system is

$$\begin{aligned}\dot{\tilde{R}}(t) &= {}^N_i\dot{R}^T(t)^N_i\hat{R}(t) + {}^N_i R^T(t)^N_i\dot{\hat{R}}(t)\\ &= -\mathcal{J}\left({}^i w_v(t)\right)\tilde{R}(t)\\ &\quad + \tilde{R}(t)\mathcal{J}\left(\tilde{x}(t) + \tilde{z}(t) + {}^i w_e(t) - {}^i w_b\right.\\ &\quad \left. - {}^N_i\hat{R}^T(t)^N w_E\right).\end{aligned} \tag{81}$$

Using the property $\mathcal{J}(v)R = R\mathcal{J}(R^T v)$ for $v \in \mathbb{R}^3$ and $R \in SO(3)$, (81) becomes

$$\begin{aligned}\dot{\tilde{R}}(t) &= \tilde{R}(t)\mathcal{J}\left(\tilde{x}(t) + \tilde{z}(t) + {}^i w_e(t) - {}^i w_b\right.\\ &\quad \left. - \tilde{R}^T(t)^i w_E(t) - \tilde{R}^T(t)^i w_v(t)\right)\\ &= \tilde{R}(t)\mathcal{J}\left(\tilde{x}(t) + \tilde{z}(t) + {}^i w_{Ev}(t) - \tilde{R}^T(t)^i w_{Ev}(t)\right)\end{aligned} \tag{82}$$

where

$${}^i w_{Ev}(t) = {}^i w_E(t) + {}^i w_v(t). \tag{83}$$

5.6 Stability

Consider the Lyapunov function candidate

$$V = \frac{1}{2}\tilde{q}^T(t)\tilde{q}(t) \tag{84}$$

where V is a smooth, positive definite function by construction and $\tilde{q}(t)$ defined in (7). Note that in the following stability proof, the fact $\mathcal{J}(v)v = 0\ \forall v \in \mathbb{R}^3$, and consequently $q^T A^{-1}(q) = q^T$ is used repeatedly.

Differentiating (84) yields

$$\dot{V} = \tilde{q}^T(t)\dot{\tilde{q}}(t). \tag{85}$$

Substituting (15) into (85) results in

$$\dot{V} = \tilde{q}^T(t)\left(A^{-1}\left(\tilde{q}(t)\right)\mathcal{J}^{-1}\left(\tilde{R}^T(t)\dot{\tilde{R}}(t)\right)\right), \tag{86}$$

and substituting (12) and (82) into (86) results in

$$\dot{V} = \tilde{q}^T(t)\left(\tilde{x}(t) + \tilde{z}(t) + {}^i w_{Ev}(t) - \tilde{R}^T(t)^i w_{Ev}(t)\right). \tag{87}$$

Substituting (4) into (87) yields

$$\begin{aligned}\dot{V} &= \tilde{q}^T(t)\left(\tilde{x}(t) + \tilde{z}(t) + {}^i w_{Ev}(t)\right.\\ &\quad \left. - \left(I - \gamma(t)\mathcal{J}\left(\tilde{q}(t)\right) + \kappa(t)\mathcal{J}^2\left(\tilde{q}(t)\right)\right){}^i w_{Ev}(t)\right)\\ &= \tilde{q}^T(t)\left(\tilde{x}(t) + \tilde{z}(t) + {}^i w_{Ev}(t) - {}^i w_{Ev}(t)\right)\\ &= \tilde{q}^T(t)\left(\tilde{x}(t) + \tilde{z}(t)\right).\end{aligned} \tag{88}$$

Substituting (77), (78), into (88) yields

$$\begin{aligned}\dot{V} &= k_x(t)\tilde{q}^T(t)\mathcal{J}\left({}^i x(t)\right){}^N_i\hat{R}^T(t)^N x\\ &\quad + k_z(t)\tilde{q}^T(t)\mathcal{J}\left((I - P(t))\,{}^i z(t)\right){}^N_i\hat{R}^T(t)^N z\\ &= k_x(t)\tilde{q}^T(t)\mathcal{J}\left({}^i x(t)\right)\tilde{R}^T(t)^i x(t)\\ &\quad + k_z(t)\tilde{q}^T(t)\mathcal{J}\left({}^i z(t)\right)\tilde{R}^T(t)^i z(t)\\ &\quad - k_z(t)\tilde{q}^T(t)\mathcal{J}\left({}^i\bar{x}(t)^i\bar{x}^T(t)^i z(t)\right)\tilde{R}^T(t)^i y(t).\end{aligned} \tag{89}$$

Note that since x is perpendicular to z, ${}^i x^T(t)^i z(t) = 0$. Thus, (89) becomes:

$$\begin{aligned}\dot{V} &= k_x(t)\tilde{q}^T(t)\mathcal{J}\left({}^i x(t)\right)\tilde{R}^T(t)^i x(t)\\ &\quad + k_z(t)\tilde{q}^T(t)\mathcal{J}\left({}^i z(t)\right)\tilde{R}^T(t)^i z(t).\end{aligned} \tag{90}$$

Using the fact that $q(t)^T\mathcal{J}\left(x(t)\right)\mathcal{J}^2\left(q(t)\right)x(t) = 0$ and substituting (4) into (90) yields

$$\begin{aligned}\dot{V} &= -k_x(t)\tilde{\gamma}(t)\tilde{q}^T(t)\mathcal{J}\left({}^i x(t)\right)\mathcal{J}\left(\tilde{q}(t)\right){}^i x(t)\\ &\quad - k_z(t)\tilde{\gamma}(t)\tilde{q}^T(t)\mathcal{J}\left({}^i z(t)\right)\mathcal{J}\left(\tilde{q}(t)\right){}^i z(t)\\ &= -k_x(t)\tilde{\gamma}(t)\|\mathcal{J}\left({}^i x(t)\right)\tilde{q}(t)\|^2\\ &\quad - k_z(t)\tilde{\gamma}(t)\|\mathcal{J}\left({}^i z(t)\right)\tilde{q}(t)\|^2\\ &< 0\end{aligned} \tag{91}$$

where $\gamma(t)$ is defined in (5). Thus, the time derivative of the Lyapunov function is locally negative definite and the observer is locally asymptotically stable.

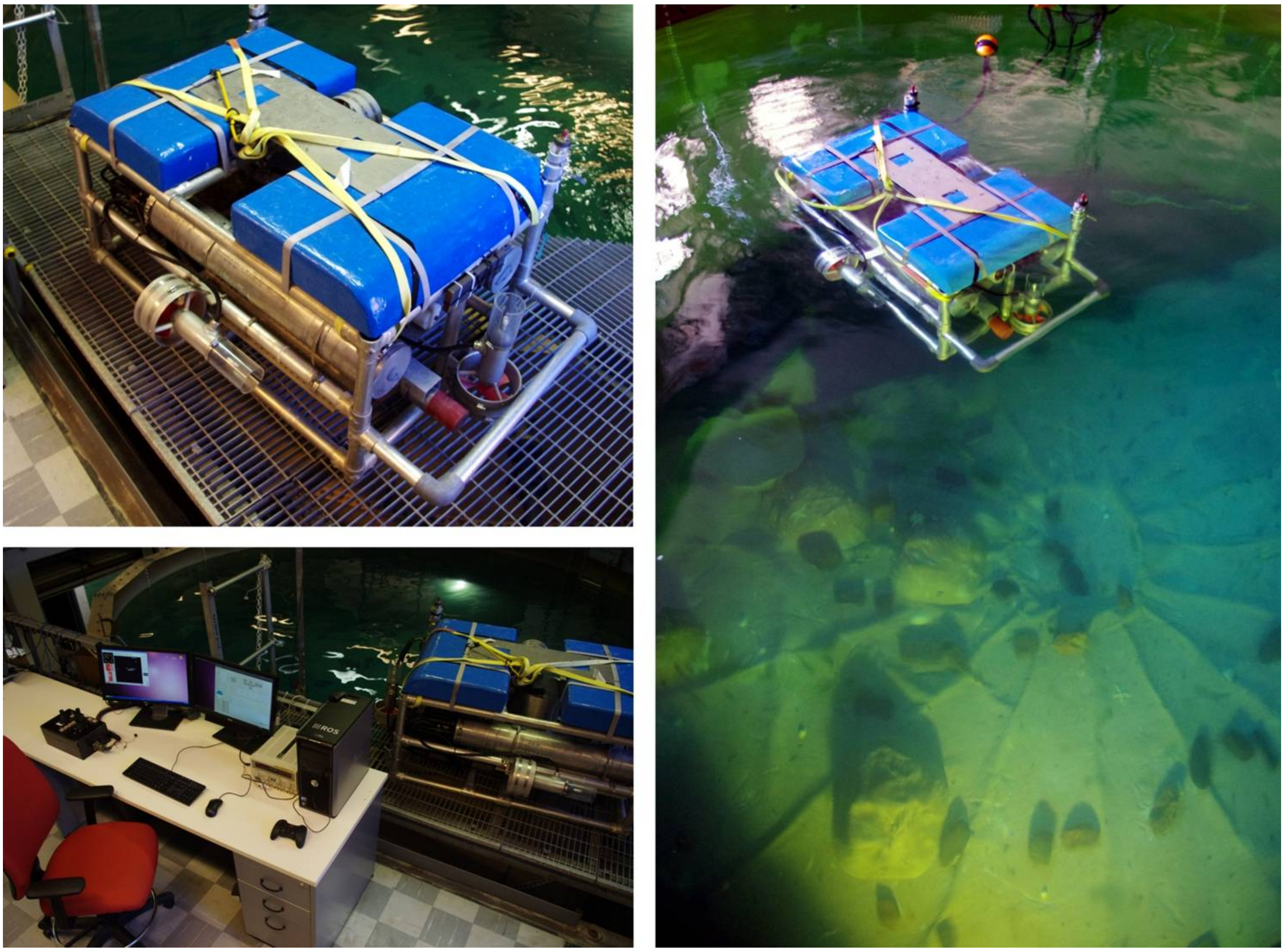

Figure 4. The Johns Hopkins University Hydrodynamic Test Facility and the fully actuated JHU ROV used during vehicle trials.

6 Gyrocompass System

The gyrocompass system is comprised of the bias (Section 4) and attitude (Section 5) observers. The estimates of ${}^{i}e(t)$, ${}^{i}w_b$, and ${}^{i}a_b$ from the bias observer presented in Section 4 are utilized in real-time by the attitude observer of Section 5 as follows:

$$
\begin{aligned}
{}^{N}x &= -\left(I_{3\times 3} + \frac{1}{g_0}\mathcal{J}({}^{N}w_E)^2\right)\mathbf{e}_3, && (92)\\
{}^{N}z &= \mathcal{J}\left({}^{N}w_E\right){}^{N}x, && (93)\\
\mathbf{e}_3 &= \left[\begin{array}{ccc} 0 & 0 & 1 \end{array}\right]^T, && (94)\\
{}^{i}x(t) &= {}^{i}a_e(t) - {}^{i}\hat{a}_b(t), && (95)\\
{}^{i}z(t) &= {}^{i}\hat{e}(t), && (96)\\
{}^{i}w_b &= {}^{i}\hat{w}_b(t) && (97)
\end{aligned}
$$

where g_0 is the magnitude of the local gravity field (~ 9.81 m/s^2).

The combined use of the reported East and bias observer (for accelerometers and angular rate sensor bias calibration on-the-fly) and the reported attitude observer will be termed the "gyrocompass system" in the following sections. Figure 3 shows a block diagram of the gyrocompass system.

7 Gyrocompass System Evaluation

The gyrocompass system is preliminarily evaluated in three numerical simulations and one UV experimental trial.

Note that in the derivation and stability proofs presented in Sections 4 and 5, the noise free case (26-28) of the measurement model is used. In the evaluation of the gyrocompass system, actual noisy sensor measurements (27-29) are used.

7.1 Test Facility

An experimental trial was performed with a remotely operated vehicle (ROV) equipped with a KVH 1775 FOG IMU (KVH Industries, Inc., Middletown, RI, USA) in the facility's 7.5 m diameter $\times$ 4 m deep fresh water tank. The ROV is a fully actuated (six-DOF) vehicle with six 1.5 kW DC brushless electric thrusters and employs a suite of sensors commonly employed on deep submergence underwater vehicles. This includes a high-end INS, the iXBlue PHINS III (iXBlue SAS, Cedex, France) (iXblue SAS, Cedex, France (2008); IXSEA (2008)), that is used as a "ground-truth" comparison during the experimental trial. The PHINS is a high-end INS (~\$120k) with roll, pitch, heading accuracies of $0.01°$, $0.01°$, $0.05°/\cos(\text{latitude})$, respectively (iXblue SAS, Cedex, France (2008)). Figure 4 shows the test facility and the ROV operating in the test tank.

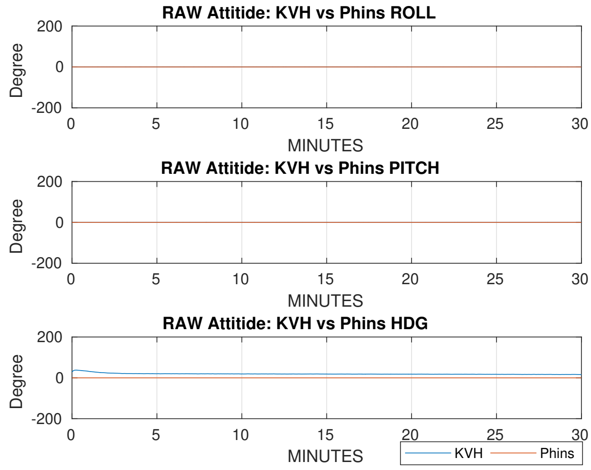

(a) Comparison between **sim1** KVH simulation and PHINS ground truth attitude.

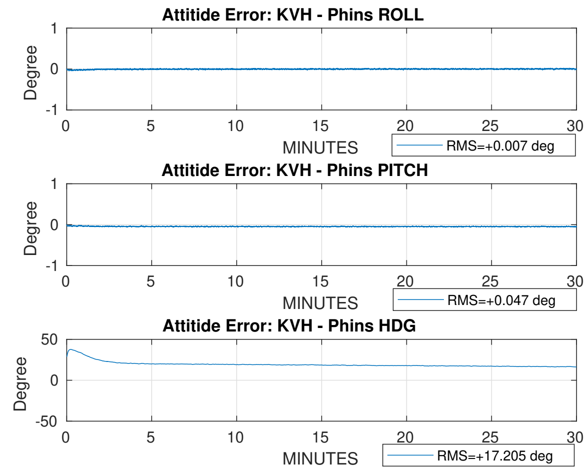

(b) **Sim1** KVH simulation attitude error.

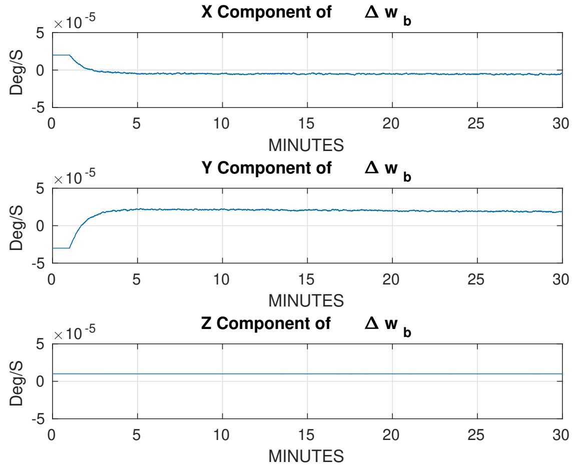

(c) **Sim1** estimated angular rate bias errors.

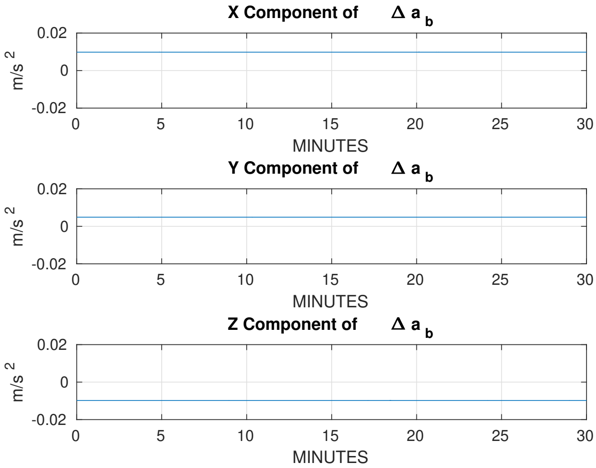

(d) **Sim1** estimated linear acceleration bias errors.

Figure 5. **Sim1** simulation results. During the simulation, the instrument experienced no instrument rotation.

7.2 Gain Selection

As with most adaptive systems that rely on persistence of excitation (Narendra and Annaswamy (1989); Sastry and Bodson (1989)) to converge to the true parameter values, the rate of convergence is dependent on the amount of excitation the system is experiencing and observer gains. In order to choose the gyrocompass gains, a constrained optimization using MATLAB's nonlinear programing solver fmincon was used to select gains for the sensor bias and East observer.

The optimization was setup as follows:

- The $k_x(t) = 1$ and $k_y(t) = 1$ gains were held constant since these attitude observer gains are easy to tune by hand.
- The k_a, k_e, k_{b_w}, and k_{b_a} gains from the sensor bias and East observer are the parameters optimized over.
- Root mean square error (RMSE) of the roll, pitch, and heading from the gyrocompass system is the function optimized.
- A 30 minute long simulation sampled at 10Hz with $\|{}^i a_v(t)\| = 0$ was used. Note that the simulation was sampled at 10hz to allow the optimization to run faster and that this simulation experienced different instrument rotations than the simulations and vehicle trial presented in Sections 7.3-7.6.
- RMSE was started to be calculated 10 minutes after filter starts.
- Initial conditions were

$$k_a = 5.0 \cdot 10^{-1} \tag{98}$$
$$k_e = 1.0 \cdot 10^{-3} \tag{99}$$
$$k_{b_w} = 1.0 \cdot 10^{-5} \tag{100}$$
$$k_{b_a} = 5.0 \cdot 10^{-1}. \tag{101}$$

These were chosen from previous experience with these gains working well.

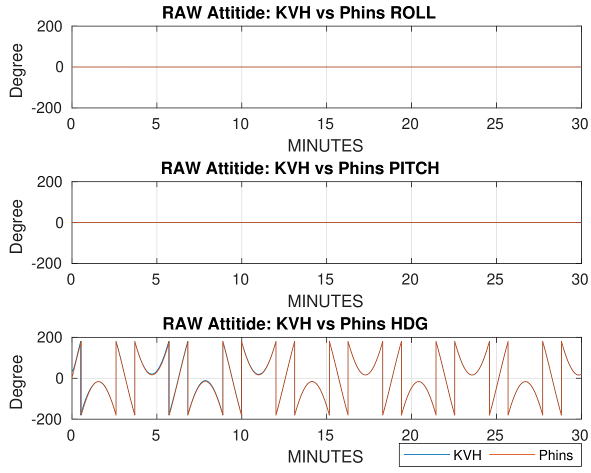

(a) Comparison between **sim2** KVH simulation and PHINS ground truth attitude.

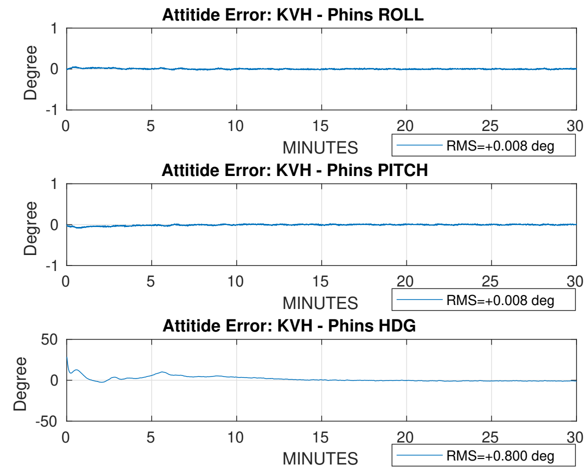

(b) **Sim2** KVH simulation attitude error.

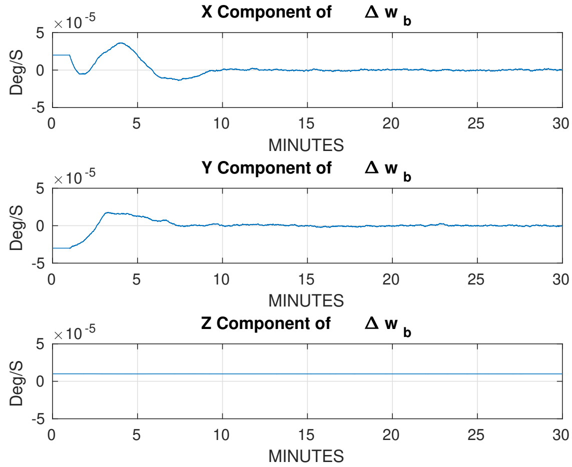

(c) **Sim2** estimated angular rate bias errors.

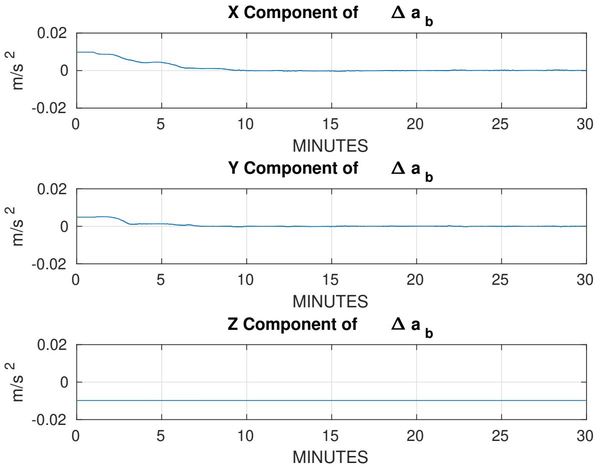

(d) **Sim2** estimated linear acceleration bias errors.

Figure 6. **Sim2** simulation results. During the simulation, the instrument experienced changes in heading.

- The constraints on the gain values were

$$0 < k_a < 10 \tag{102}$$
$$0 < k_e < 1 \tag{103}$$
$$0 < k_{b_w} < 1 \tag{104}$$
$$0 < k_{b_a} < 1 \tag{105}$$

The gains resulting from the optimization are

$$k_a = 3.3 \cdot 10^{-1} \tag{106}$$
$$k_e = 1.2 \cdot 10^{-3} \tag{107}$$
$$k_{b_w} = 1.5 \cdot 10^{-5} \tag{108}$$
$$k_{b_a} = 8.0 \cdot 10^{-1} \tag{109}$$
$$k_x(t) = 1 \tag{110}$$
$$k_y(t) = 1 \tag{111}$$

where $k_x(t)$ and $k_y(t)$ are the static gains chosen for the attitude observer. These gains were used during the simulations and vehicle experiment presented in this paper. We note that this gain optimization process did not result in gains that were significantly different from the initial gains that we manually selected, and did not result in significant improvements in observer performance.

Note: During the simulations and vehicle experiment, we gain-scheduled the sensor bias gains, k_{b_w} and k_{b_a}, by setting them to zero for the first minute of operation to allow the ${}^i\hat{e}(t)$ and ${}^i\hat{a}_e(t)$ signals to settle so that the sensor bias estimates are not driven far from their true values during the start-up transient period.

7.3 Simulation Setup

The gyrocompass system is evaluated in three numerical simulations.

- Sensor measurement sampling was simulated at 1kHz.
- Simulations include sensor biases consistent in magnitude to those seen in KVH 1775 IMUs.
- Simulations were for a latitude of 39.32°N.
- $\|{}^i a_v(t)\| = 0$ for the three simulations.

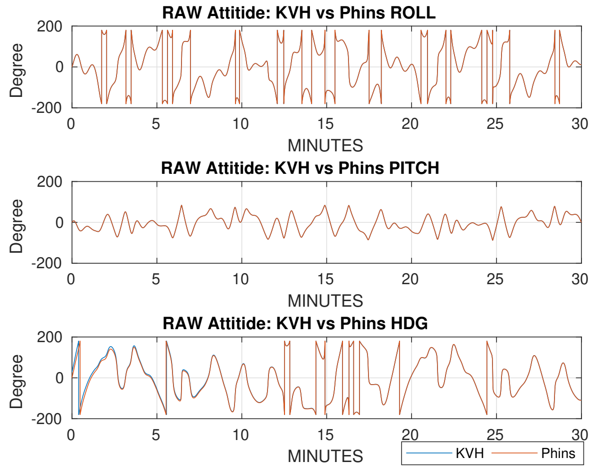

(a) Comparison between **sim3** KVH simulation and PHINS ground truth attitude.

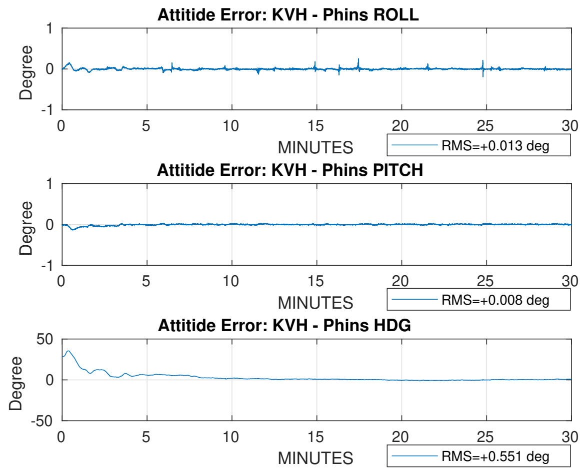

(b) **Sim3** KVH simulation attitude error.

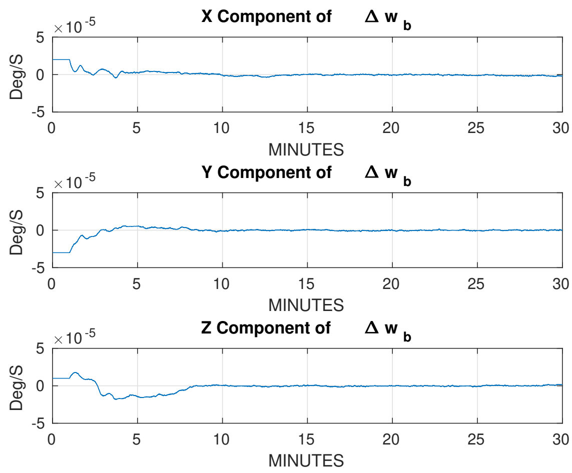

(c) **Sim3** estimated angular rate bias errors.

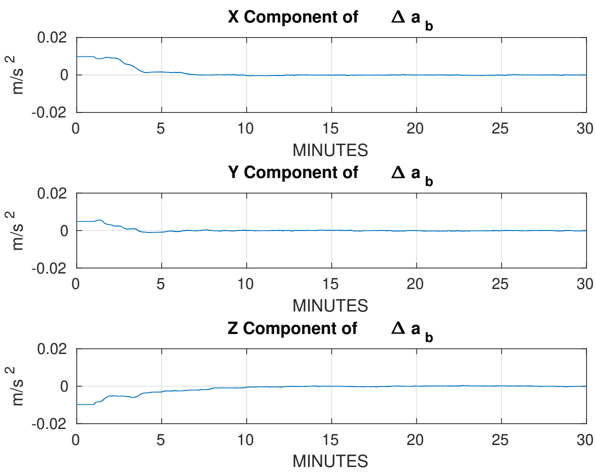

(d) **Sim3** estimated linear acceleration bias errors.

Figure 7. **Sim3** simulation results. During the simulation, the instrument experienced changes in heading, roll, and pitch.

- Simulations included sensor measurements with sensor noise representative of the KVH 1775 FOG IMU (used ${}^{i}a_m(t)$ and ${}^{i}w_m(t)$ instead of ${}^{i}a_e(t)$ and ${}^{i}w_e(t)$). Angular velocity sensor and linear accelerometer sensor noises are computed from the IMU's specifications KVH Industries, Inc., Middletown, RI, USA (2015), as per Woodman (2007), and confirmed by the authors experimentally to be $\sigma_w = 6.32 \times 10^{-3}$ rad/s and $\sigma_a = 0.0037$ g.
- The sensor biases used in the three simulations are:

$$w_b = \begin{bmatrix} -2 & 3 & -1 \end{bmatrix}^T \cdot 10^{-5} \; rad/s \tag{112}$$

$$a_b = \begin{bmatrix} 1 & -0.5 & 1 \end{bmatrix}^T \cdot 10^{-3} \; g \tag{113}$$

- The **sim1** simulation experienced no rotation.
- The **sim2** simulation experienced changes in heading.
- The **sim3** simulation experienced changes in heading, roll, and pitch.
- Root mean square error (RMSE) was started to be calculated 20 minutes after filter starts.
- The initial condition, ${}^{N}_{i}\hat{R}(t)$, is chosen such that the initial heading is off by $\sim 30 - 35°$. This is an initial heading that can be easily achieved with magnetic compasses. In the future, we plan to use the magnetometer in the KVH IMU for choosing the initial condition of the proposed gyrocompass system.
- The sensor biases estimates, ${}^{i}\hat{w}_b(t)$ and ${}^{i}\hat{a}(t)$, were all set to zero for their initial conditions.

7.4 Simulation Results

The estimated attitude and sensor bias errors for the three simulations are shown in Figures 5-7. The **sim1** simulation results show that when the instrument is not excited via rotations, the gyrocompass system bias estimates and attitude estimates do not converge to their true values. This is consistent with adaptive identifiers which rely on persistence of excitation (Narendra and Annaswamy (1989); Sastry

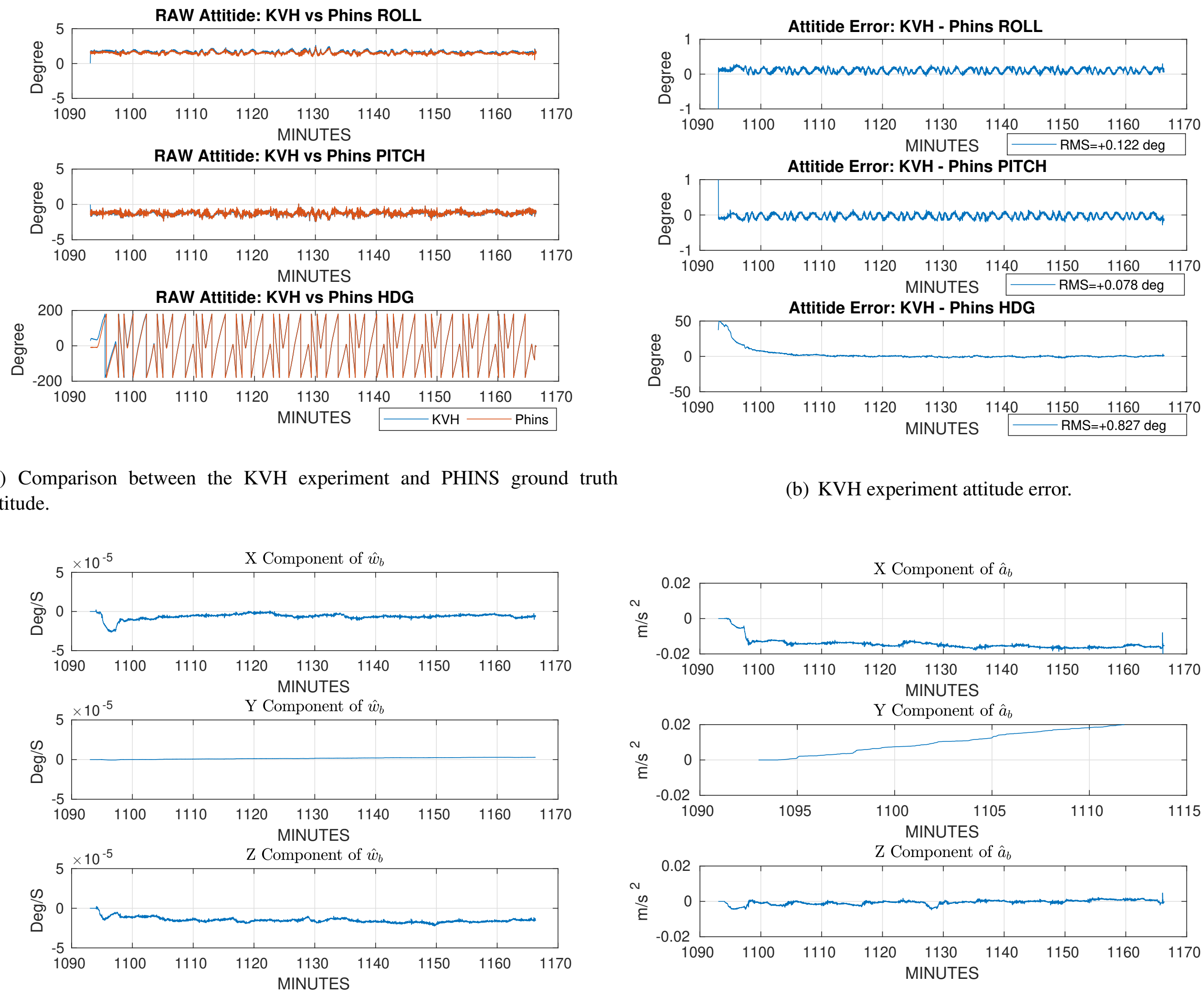

(a) Comparison between the KVH experiment and PHINS ground truth attitude.

(b) KVH experiment attitude error.

(c) Estimated angular rate biases.

(d) Estimated linear acceleration biases.

Figure 8. Results from a full-scale vehicle trial in the JHU Hydrodynamic Laboratory's test tank. During the experiment, the vehicle experienced changes in heading.

and Bodson (1989)). In the **sim2** and **sim3** simulations, the attitude converges. Specifically, the simulations show (after the system has converged) the gyrocompass system to estimate roll and pitch within $0.1°$ and heading within $1°$ in RMSE. The **sim3** simulation converges faster than the **exp2** simulation due to the increased excitation experienced by the instrument in the **sim3** simulation.

In simulations with no sensor noise (not shown), we observed the attitude and bias errors estimations errors to converge to zero. In the three simulations reported herein, which include simulated sensor noise for the gyros and accelerometers, we see the attitude estimation errors converge to a neighborhood zero. As shown in the stability proof, the convergence of the bias estimation error is seen to depend upon the richness of the attitude excursions (persistence of excitation) the IMU experiences: In simulation **sim1**, where the IMU is motionless, the bias estimates do not converge to the true bias values. In simulation **sim2**, where the IMU experiences excursions in heading, with roll and pitch remaining zero, only four of the six components of the bias estimate converge to the neighborhood of the true values. In simulation **sim3**, where the IMU experiences attitude excursions in 3-DOF, all six bias estimate terms converge to the "true" bias values.

It is important to note that the ${}^i\hat{w}_b(t)$ and ${}^i\hat{a}_b(t)$ update laws do not update bias components in the kernels of $\mathcal{J}\left({}^i a_e(t)\right)$ and $\mathcal{J}\left({}^i w_e(t)\right)$ respectively. Thus, in the case of **sim2** where the instrument only experiences changes in heading (the PE condition for asymptotic stability is not met when the instrument only experiences heading changes), the components of the biases along the gravity vector do not evolve. This configuration is common in oceanographic UVs which are commonly passively stable in roll and pitch. Since the convergence of ${}^i\hat{e}(t)$ is dependent on accurate estimation of the components of the biases in the North-East plane, the gyrocompass system is still able to converge to the correct attitude in **sim2** (only heading changes) since the components of the biases which affect the accuracy of the "East" estimate are properly estimated. Thus, in vehicles like oceanographic UVs which are passively stable in roll and pitch, it is not necessary to estimate accurately the

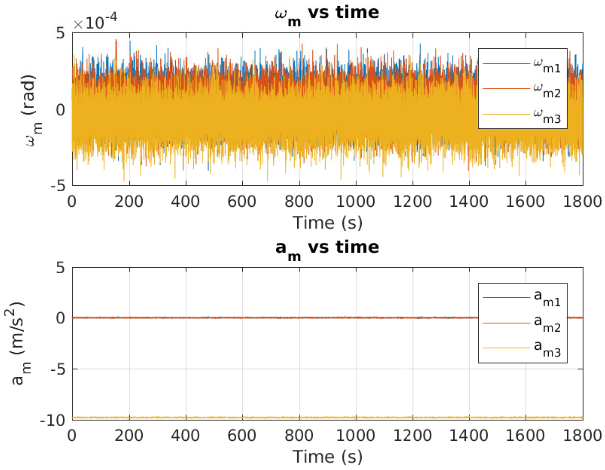

(a) **sim1** KVH simulation measurements.

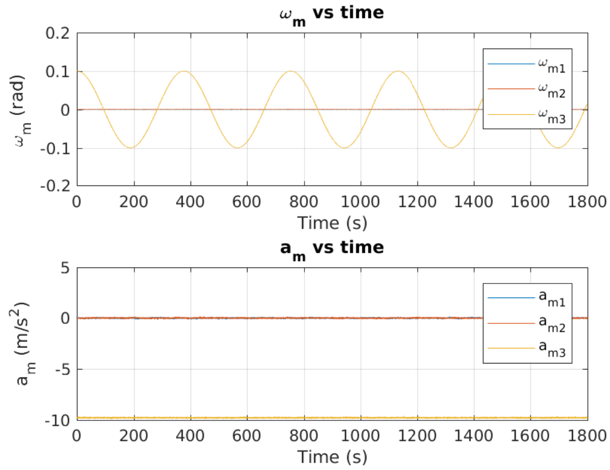

(b) **sim2** KVH simulation measurements.

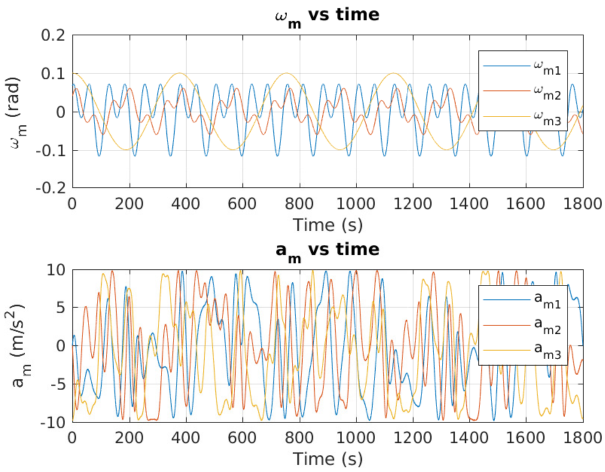

(c) **sim3** KVH simulation measurements.

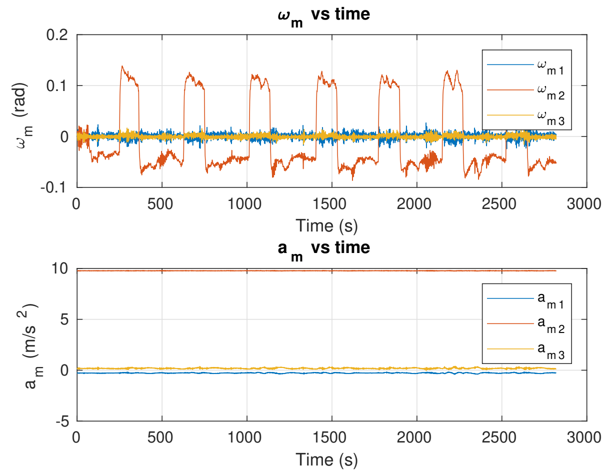

(d) Vehicle trial KVH measurements.

Figure 9. Instrument measurements from the three simulations and one vehicle trial. Note that all the signals are in the instrument frame (i.e. ${}^i w_m(t), {}^i a_m(t)$).

components of the biases along the gravity vector in order to achieve accurate true-North attitude estimation.

7.5 Experimental Setup

The gyrocompass system is evaluated with a preliminary vehicle trial employing a comparatively low-cost ($\sim$ \$20k USD) FOG KVH 1775 IMU (KVH Industries, Inc., Middletown, RI, USA).

- The KVH 1775 FOG IMU was sampled at 5kHz.
- The KVH 1775 FOG IMU was aligned via a fixture to the ROV's iXBLUE PHINS INS (iXblue SAS, Cedex, France). The PHINS attitude is used as ground truth during our experimental evaluation of the attitude estimator.
- The **KVH** experiment was conducted at a latitude of 39.32°N.
- The ROV was commanded to execute smooth sinusoidal rotations ($\sim 720°$) in heading while in closed-loop control.
- The ROV experienced $\|{}^i a_v(t)\| \approx 0$ during the experiment.
- RMSE error was started to be calculated 20 minutes after filter starts.
- The initial condition, ${}^N_i\hat{R}(t)$, is chosen such that the initial heading is off by $\sim 40°$. This is an initial heading that can be easily achieved with magnetic compasses. In the future, we plan to use the magnetometer in the KVH IMU for choosing the initial condition of the proposed gyrocompass system.
- The sensor biases estimates, ${}^i\hat{w}_b(t)$ and ${}^i\hat{a}(t)$, were all set to zero for their initial conditions.
- The instrument is mounted on the vehicle such that the instrument's x-axis is toward starboard, the y-axis is toward up, and the z-axis is toward stern of the vehicle.

7.6 Experimental Results

The attitude and sensor bias estimations and attitude errors for the vehicle trial are shown in Figure 8. The results show that during this experimental evaluation of the gyrocompass system, the attitude estimate converged to the true attitude. Roll and pitch converged to within $0.15°$ RMSE and true-North heading to within $1°$ RMSE of their true values.

In this experiment, where the vehicle and IMU principally experienced excursions in heading, with vehicle's roll and pitch remaining passively stable near zero, we see that the attitude estimation errors converge to a neighborhood zero and four of the six bias estimate terms converge to steady values. Thus the experimental conditions and experimental results of the bias and attitude estimator are seen to be similar to that observed in the simulation study **sim2**.

Note that as in **sim2**, the JHU ROV is a passively in roll and pitch and predominantly experiences attitude changes in heading only. Hence, while the components of the biases along the gravity vector (along the IMU's y-axis) do not converge to their correct values (See Figure 8), the true-North attitude does converge to the correct attitude.

In this preliminary result, the estimator took $\sim$15 minutes to converge to the correct true-North heading. Long convergence time is typical of true-North gyrocompass systems. For example, the iXBlue PHINS takes $\sim$10 minutes to achieve fine alignment IXSEA (2008). We are currently investigating improvements to this sensor bias and East observer (e.g. adaptive gains) to improve its rate of convergence.

8 Conclusion

This paper reports the derivation and stability analysis of an adaptive bias and East vector observer and an attitude observer for use in true-North gyrocompass systems. Preliminary simulations and a full-scale vehicle experiment using a commercially available low-cost FOG IMU are reported.

The preliminary simulation and vehicle trial suggest, for the case of a gyrocompass system that experiences rotations, the convergence of the reported gyrocompass system to the true attitude *without* using magnetometers. The vehicle trial shows roll and pitch converge to within $0.15°$ RMSE and true-North heading to within $1°$ RMSE of their true values.

In future studies, the authors hope to improve the time of convergence, increase the accuracy of the gyrocompass system, extend the system to account for nontrivial vehicle accelerations, and conduct extensive full-scale experimental vehicle trials both in the lab and in the field.

Acknowledgements

We are grateful to Abhimanyu Shah for his help in checking and proofreading the manuscript and gratefully acknowledge the support of the National Science Foundation under NSF award OCE-1435818. We are grateful to the anonymous reviewers who provided exceptionally cogent and insightful comments and suggestions.

References

Alonso R and Shuster MD (2002a) TWOSTEP: A fast robust algorithm for attitude-independent magnetometer-bias determination. *Journal of the Astronautical Sciences* 50(4): 433–452.

Alonso R and Shuster MD (2002b) Complete linear attitude-independent magnetometer calibration. *Journal of the Astronautical Sciences* 50(4): 477–490.

Batista P, Silvestre C and Oliveira P (2019) Attitude observer on the special orthogonal group with earth velocity estimation. *Systems & Control Letters* 126: 33–39. DOI:https://doi.org/10.1016/j.sysconle.2019.03.001. URL http://www.sciencedirect.com/science/article/pii/S0167691119300301.

Besançon G (2000) Remarks on nonlinear adaptive observer design. *Systems & Control Letters* 41(4): 271 – 280.

Chirikjian GS (2011) *Stochastic Models, Information Theory, and Lie Groups, Volume 2: Analytic Methods and Modern Applications*, volume 2. Springer Science & Business Media.

Clegg D and Peterson M (2003) User Operational Evaluation System of Unmanned Underwater Vehicles for very Shallow Water Mine Countermeasures. In: *OCEANS 2003*, volume 3. pp. 1417–1423.

Clem TR, Sternlicht DD, Fernandez JE, Prater JL, Holtzapple R, Gibson RP, Klose JP and Marston TM (2012) Demonstration of advanced sensors for underwater unexploded ordnance (UXO) detection. In: *OCEANS 2012*. pp. 1–4.

Costanzi R, Fanelli F, Monni N, Ridolfi A and Allotta B (2016) An Attitude Estimation Algorithm for Mobile Robots Under Unknown Magnetic Disturbances. *IEEE/ASME Transactions on Mechatronics* 21(4): 1900–1911.

Crassidis JL, Lai KL and Harman RR (2005) Real-time attitude-independent three-axis magnetometer calibration. *Journal of Guidance, Control, and Dynamics* 28(1): 115–120.

Crassidis JL, Markley FL and Cheng Y (2007) Survey of nonlinear attitude estimation methods. *Journal of guidance, control, and dynamics* 30(1): 12–28.

Gambhir B (1975) Determination of magnetometer biases using module RESIDG. *Computer Sciences Corporation, Report* (3000-32700): 01.

George M and Sukkarieh S (2005) Tightly coupled INS/GPS with bias estimation for UAV applications. In: *Proceedings of Australiasian Conference on Robotics and Automation (ACRA)*.

Guo P, Qiu H, Yang Y and Ren Z (2008) The soft iron and hard iron calibration method using extended Kalman filter for attitude and heading reference system. In: *Position, Location and Navigation Symposium, 2008 IEEE/ION*. IEEE, pp. 1167–1174.

Hamel T and Mahony R (2006) Attitude estimation on SO(3) based on direct inertial measurements. In: *2006 IEEE International Conference on Robotics and Automation (ICRA)*. IEEE, pp. 2170–2175.

iXblue SAS, Cedex, France (2008) iXSEA PHINS INS datasheet.

IXSEA (2008) *PHINS III User Guide*. IXSEA, MU-PHINSIII-006 B edition.

Khalil HK (1996) *Noninear Systems*. Prentice-Hall, New Jersey.

Kinsey JC and Whitcomb LL (2004) Preliminary field experience with the DVLNAV integrated navigation system for oceanographic submersibles. *Control Engineering Practice* 12(12): 1541 – 1549. Guidance and control of underwater vehicles.

Kinsey JC and Whitcomb LL (2007) Adaptive Identification on the Group of Rigid-Body Rotations and its Application to Underwater Vehicle Navigation. *IEEE Transactions on*

Robotics 23(1): 124–136.

Kok M, Hol JD, Schön TB, Gustafsson F and Luinge H (2012) Calibration of a magnetometer in combination with inertial sensors. In: *Information Fusion (FUSION), 2012 15th International Conference on*. IEEE, pp. 787–793.

KVH Industries, Inc, Middletown, RI, USA (2015) KVH 1775 IMU datasheet.

Li X and Li Z (2012) A new calibration method for tri-axial field sensors in strap-down navigation systems. *Measurement Science and technology* 23(10): 105105.

Mahony R, Hamel T and Pflimlin JM (2008) Nonlinear Complementary Filters on the Special Orthogonal Group. *IEEE Transactions on Automatic Control* 53(5): 1203–1218.

Martinelli A (2012) Vision and IMU Data Fusion: Closed-Form Solutions for Attitude, Speed, Absolute Scale, and Bias Determination. *IEEE Transactions on Robotics* 28(1): 44–60.

Metni N, Pflimlin JM, Hamel T and Soueres P (2005) Attitude and gyro bias estimation for a flying UAV. In: *2005 IEEE/RSJ International Conference on Intelligent Robots and Systems (IROS)*. pp. 1114–1120.

Metni N, Pflimlin JM, Hamel T and Soures P (2006) Attitude and gyro bias estimation for a VTOL UAV. *Control Engineering Practice* 14(12): 1511 – 1520.

Murray RM, Li Z and Sastry SS (1994) *A Mathematical Introduction to Robotic Manipulation*. Boca Raton: CRC Press.

Narendra KS and Annaswamy AM (1989) *Stable adaptive systems*. Prentice-Hall Inc.

Packard GE, Kukulya A, Austin T, Dennett M, Littlefield R, Packard G, Purcell M, Stokey R and Skomal G (2013) Continuous autonomous tracking and imaging of white sharks and basking sharks using a REMUS-100 AUV. In: *2013 OCEANS - San Diego*. pp. 1–5.

Pflimlin JM, Hamel T and Soures P (2007) Nonlinear attitude and gyroscope's bias estimation for a VTOL UAV. *International Journal of Systems Science* 38(3): 197–210.

Rugh WJ (1996) *Linear System Theory (2Nd Ed.)*. Upper Saddle River, NJ, USA: Prentice-Hall, Inc. ISBN 0-13-441205-2.

Sastry S and Bodson M (1989) *Adaptive control: stability, convergence and robustness*. Prentice-Hall Inc.

Scandaroli GG and Morin P (2011) Nonlinear filter design for pose and IMU bias estimation. In: *2011 IEEE International Conference on Robotics and Automation (ICRA)*. pp. 4524–4530.

Scandaroli GG, Morin P and Silveira G (2011) A nonlinear observer approach for concurrent estimation of pose, IMU bias and camera-to-IMU rotation. In: *2011 IEEE/RSJ International Conference on Intelligent Robots and Systems (IROS)*. pp. 3335–3341.

Spielvogel AR and Whitcomb LL (2015) Preliminary results with a low-cost fiber-optic gyrocompass system. In: *2015 OCEANS*. pp. 1–5.

Spielvogel AR and Whitcomb LL (2017a) A stable adaptive attitude estimator on SO(3) for true-North seeking gyrocompass systems: Theory and preliminary simulation evaluation. In: *2017 IEEE International Conference on Robotics and Automation (ICRA)*. pp. 3231–3236.

Spielvogel AR and Whitcomb LL (2017b) Adaptive estimation of measurement bias in six degree of freedom inertial measurement units: Theory and preliminary simulation evaluation. In: *2017 IEEE/RSJ International Conference on Intelligent Robots and Systems (IROS)*. pp. 5880–5885.

Spielvogel AR and Whitcomb LL (2018) Adaptive Sensor Bias Estimation in Nine Degree of Freedom Inertial Measurement Units: Theory and Preliminary Evaluation. In: *2018 IEEE/RSJ International Conference on Intelligent Robots and Systems (IROS)*. pp. 5555–5561.

Spielvogel AR and Whitcomb LL (2018) Adaptive Bias and Attitude Observer on the Special Orthogonal Group for True-North Gyrocompass Systems: Theory and Preliminary Results. In: *Proceedings of Robotics: Science and Systems*. Pittsburgh, Pennsylvania.

Steele E, Boyd T, Inall M, Dumont E and Griffiths C (2012) Cooling of the West Spitsbergen Current: AUV-based turbulence measurements west of Svalbard. In: *2012 IEEE/OES Autonomous Underwater Vehicles (AUV)*. pp. 1–7.

Troni G and Whitcomb LL (2013) Adaptive Estimation of Measurement Bias in Three-Dimensional Field Sensors with Angular Rate Sensors: Theory and Comparative Experimental Evaluation. In: *Robotics: Science and Systems*.

Troni G and Whitcomb LL (2019) Field Sensor Bias Calibration With Angular-Rate Sensors: Theory and Experimental Evaluation With Application to Magnetometer Calibration. *IEEE/ASME Transactions on Mechatronics* 24(4): 1698–1710. DOI:10.1109/TMECH.2019.2920367.

Woodman OJ (2007) An introduction to inertial navigation. Technical report, University of Cambridge, Cambridge, UK.

Wu TH, Kaufman E and Lee T (2015) Globally Asymptotically Stable Attitude Observer on SO(3). In: *2015 54th IEEE Conference on Decision and Control (CDC)*. pp. 2164–2168.

Zhou M, Bachmayer R and de Young B (2014) Working towards seafloor and underwater iceberg mapping with a Slocum glider. In: *2014 IEEE/OES Autonomous Underwater Vehicles (AUV)*. pp. 1–5.

Appendix 1: Lemma 1 Proof

Lemma 1: Given a system of the following form:

$$\dot{x}(t) = A(t)x(t) + f(t) \tag{114}$$
$$y(t) = Cx(t) \tag{115}$$

where $x(t) \in \mathbb{R}^n$, and $y(t) \in \mathbb{R}^p$ such that

(i) $\lim_{t\to\infty} \|y(t)\| = 0$

(ii) $\lim_{t\to\infty} \|f(t)\| = 0$

(iii) $[A(t), C]$ is UCO;

then $\lim_{t\to\infty} \|x(t)\| = 0$.

Proof: The proof follows the structure of the proof of Lemma A.1 in (Besançon (2000)).

First, note that from (iii), the system

$$\dot{x}(t) = A(t)x(t) \tag{116}$$
$$y(t) = Cx(t) \tag{117}$$

is UCO. That is, $\exists \beta_1, \beta_2, \delta > 0$ such that $\forall t_0 \geq 0$, the observability grammian

$$N(t_0, \delta) = \int_{t_0}^{t_0+\delta} \Phi^T(\tau, t_0) C^T C \Phi(\tau, t_0)\, d\tau \tag{118}$$

satisfies (17).

Next, recall that the solution of the system (114) for any $t_0 \geq 0$ is given by

$$x(t) = \Phi(t, t_0)x(t_0) + \int_{t_0}^{t} \Phi(t, \tau)f(\tau)\, d\tau. \tag{119}$$

Then

$$\begin{aligned}
N(t,\delta)x(t) &= \int_{t}^{t+\delta} \Phi^T(\tau,t)C^T C\Phi(\tau,t)\, d\tau\ x(t) \\
&= \int_{t}^{t+\delta} \Phi^T(\tau,t)C^T C\Phi(\tau,t)[\Phi(t,t_0)x(t_0) \\
&\quad + \int_{t_0}^{t} \Phi(t,s)f(s)\, ds]\, d\tau \\
&= \int_{t}^{t+\delta} \Phi^T(\tau,t)C^T C[x(\tau) \\
&\quad - \int_{t}^{\tau} \Phi(\tau,s)f(s)\, ds]\, d\tau \\
&= \int_{0}^{\delta} \Phi^T(\sigma+t,t)C^T[Cx(\sigma+t) \\
&\quad - \int_{t}^{\sigma+t} C\Phi(\sigma+t,s)f(s)\, ds]\, d\sigma \\
&= \int_{0}^{\delta} \Phi^T(\sigma+t,t)C^T[y(\sigma+t) \\
&\quad - \int_{0}^{\sigma} C\Phi(\sigma+t,v+t)f(v+t)\, dv]\, d\sigma
\end{aligned} \tag{120}$$

Since

- $\Phi(\sigma+t,t)$ and $\Phi(\sigma+t,v+t)$ are bounded (from (iii)) on $[0,\delta]$,
- $\lim_{t\to\infty} y(t) = 0$,
- and $\lim_{t\to\infty} f(t) = 0$,

then

$$\lim_{t\to\infty} N(t,t+\delta)x(t) = 0. \tag{121}$$

Thus, from (121) and (iii), we can conclude that

$$\lim_{t\to\infty} \|x(t)\| = 0. \tag{122}$$

Appendix 2: Uniform Complete Observability Of The Sensor Bias and East Observer

As stated in Section 4.4, asymptotic convergence of the sensor bias and East observer to the true values is dependent on $[A(t), C]$ being uniform complete observability (UCO). However, it is not obvious that $\Phi(t, t_0)$, the transition matrix for $A(t)$, has a closed-form solution for non-trivial ${}^i w_e(t)$ and ${}^i a_e(t)$ and, in consequence, it is not clear how to prove analytically that the observability grammian

$$N(t_0,\delta) = \int_{t_0}^{t_0+\delta} \Phi^T(\tau,t_0)C^T C\Phi(\tau,t_0)\, d\tau \tag{123}$$

satisfies (17).

We have, however, verified numerically that when ${}^i w_e(t)$ and ${}^i a_e(t)$ are PE, $[A(t), C]$ is UCO. Figure 9 presents the instrument measurements from the three simulations and one vehicle trial. The following sections present results from numerically evaluating the observability grammian of the three simulations.

Sim1 Simulation

In **sim1**, ${}^i w_e(t)$ and ${}^i a_e(t)$ are constant (i.e. heading, pitch, and roll are all uniformly zero), and thus, not persistently exciting (PE). Hence, the observability grammian for $[A(t), C]$ is not full rank and $[A(t), C]$ is not UCO. Numerically, we can verify that $\text{rank}\,(N(0,60)) = 6$, $\sigma_{min}(N(0,60)) = 4.59 \times 10^{-12}$, and $\sigma_{max}(N(0,60)) = 6.96 \times 10^6$ (full rank occurs when $\text{rank}\,(N(0,60)) = 12$).

Sim2 Simulation

In **sim2**, the vehicle only experiences changes in heading only, with uniformly zero roll and pitch, and ${}^i w_e(t)$ and ${}^i a_e(t)$ are not PE. Hence, the observability grammian for $[A(t), C]$ is not full rank and $[A(t), C]$ is not UCO. Numerically, we can verify that $\text{rank}\,(N(0,60)) = 10$, $\sigma_{min}(N(0,60)) = 3.76 \times 10^{-12}$, and $\sigma_{max}(N(0,60)) = 6.90 \times 10^6$ (full rank occurs when $\text{rank}\,(N(0,60)) = 12$).

Sim3 Simulation

In **sim3**, the vehicle experiences changes in roll, pitch, and heading, and ${}^i w_e(t)$ and ${}^i a_e(t)$ are PE. The observability grammian for $[A(t), C]$ can be shown numerically to be full rank and, in consequence, $[A(t), C]$ is UCO. Numerically, we can verify that $\text{rank}\,(N(0,60)) = 12$, $\sigma_{min}(N(0,60)) = 1.04$, and $\sigma_{max}(N(0,60)) = 4.89 \times 10^6$ (full rank occurs when $\text{rank}\,(N(0,60)) = 12$).

Conclusion

We conclude from numerically evaluating the observability grammians over $t = [0,60]$ from the three simulations, that when ${}^i w_e(t)$ and ${}^i a_e(t)$ are PE (**sim3**), the observer is asymptotically stable. Note that during **sim2**, although the observability grammian is not full rank, excitement in heading (**sim2**) causes the observability grammian to be rank 10, which is a higher rank than in the case of a stationary instrument (**sim1**).